JGR Oceans

Author Contributions:

Conceptualization: Jan Hitzegrad, Nils Goseberg
Data curation: Jan Hitzegrad
Formal analysis: Jan Hitzegrad, Sebastian Köster
Funding acquisition: Nils Goseberg
Investigation: Jan Hitzegrad, Sebastian Köster
Methodology: Jan Hitzegrad, Sebastian Köster, Nils Goseberg
Project administration: Christian Windt, Nils Goseberg
Software: Jan Hitzegrad, Sebastian Köster
Supervision: Christian Windt, Nils Goseberg
Validation: Jan Hitzegrad, Sebastian Köster, Christian Windt
Visualization: Jan Hitzegrad
Writing – original draft: Jan Hitzegrad
Writing – review & editing: Jan Hitzegrad, Sebastian Köster, Christian Windt, Nils Goseberg

Understanding the Role of Sharp Edges in the Propagation of Surface Gravity Waves

**Jan Hitzegrad**[1] , **Sebastian Köster**[1], **Christian Windt**[1], **and Nils Goseberg**[1,2]

[1]Leichtweiß-Institute for Hydraulic Engineering and Water Resources, Technische Universität Braunschweig, Braunschweig, Germany, [2]Coastal Research Center, Joint Research Facility of Leibniz University Hannover and Technische Universität Braunschweig, Hannover, Germany

Abstract Ultra-rough oceanic surfaces, such as oyster reefs, are characterized by densely-packed, sharp-edged roughness elements that induce high frictional resistance on the ambient flows. To effectively employ, for example, oyster reefs as a nature-based solution in coastal protection, a detailed understanding of the frictional wave energy dissipation processes is necessary. This work reports on an experimental study in which six surrogates of very to ultra-rough oceanic bed surfaces were subjected to regular waves. The influences of different sharpness' of roughness elements (bluntly-shaped, sharp-edged, and a combination thereof) and relative spacing between elements compared to the near-bed horizontal excursion amplitude, λ/a_b, on the wave attenuation have been investigated. Turbulence is 2–27 times larger for sharp-edged surfaces and 1 to 18 times larger for mix surfaces than those of bluntly-shaped surfaces. Maximum bed shear stresses, hydraulic roughness lengths, and wave friction factors are likewise significantly larger for sharp-edged compared to bluntly-shaped surfaces. These observations indicate that the sharp edges are crucial for frictional energy dissipation. Comparing the maximum bed shear stresses determined from wave height reductions to those determined from velocity measurements indicates that in addition to turbulent kinetic energy (*TKE*), periodic form-induced stresses significantly contribute to the overall bed shear stresses. This study provides new insight into the frictional dissipation processes of oscillating flows encountering ultra-rough surfaces.

Plain Language Summary Oyster reefs and other ultra-rough bed surfaces near a shore significantly reduce wave heights of passing waves. Integrated into a nature-based coastal protection system, they can reduce the requirement for artificial structures (e.g., seawalls and breakwaters). However, the processes causing the wave height reductions have not been comprehensively investigated. Oyster reefs have ultra-rough surfaces, with edges so sharp they can cut rubber boots. As a model of those surfaces, we investigated the influence of different shapes of elements (sharp, blunt, and a combination thereof) on wave height reductions to address this feature of ultra-rough surfaces. We found that the sharp-edged elements cause significantly stronger turbulence in the surrounding flow, which leads to more substantial wave height reductions. We also found that the spacing between the elements in relation to the wave length influences the wave height reduction. Furthermore, we compared two methods of estimating the shear stress near the bed and found similar trends but different magnitudes of the results for the sharp-edged surfaces. The results improve the understanding of underlying processes of wave height reductions caused by ultra-rough bed surfaces. It is suggested to consider the bed roughness more prominently when designing oyster reefs as a coastal protection measure.

1. Introduction

Oysters, as reef-building bivalves, are important eco-engineers (Jones et al., 1994) in coastal ecosystems, whose efficiency toward nature-based coastal protection is now widely recognized (Borsje et al., 2011; Bouma et al., 2014; Morris et al., 2018; Smaal et al., 2019). Due to their ultra-rough surface, epibenthic oyster reefs exert bio-physical interactions on local hydro- and morphodynamics, influencing the environment beyond their boundaries (Dame, 2016; Walles, Salvador de Paiva, et al., 2015). Regarding coastal protection, oyster reefs are known to (a) attenuate wave energy (Manis et al., 2015; Morris et al., 2021; Wiberg et al., 2019), (b) reduce estuarine currents (Kitsikoudis et al., 2020; Styles, 2015; Whitman & Reidenbach, 2012), and (c) stabilize seabed sediments and shorelines (Chowdhury et al., 2019; Salvador de Paiva et al., 2018; Scyphers et al., 2011). Concurrently, oyster reefs provide further ecosystem services as they, for example, (a) create habitats for various species, including resident invertebrates, mobile crustaceans, and bottom-feeding fish (Grabowski et al., 2012), (b) enhance water quality through filter-feeding of suspended particles (Nelson et al., 2004; Newell, 1988) and (c)
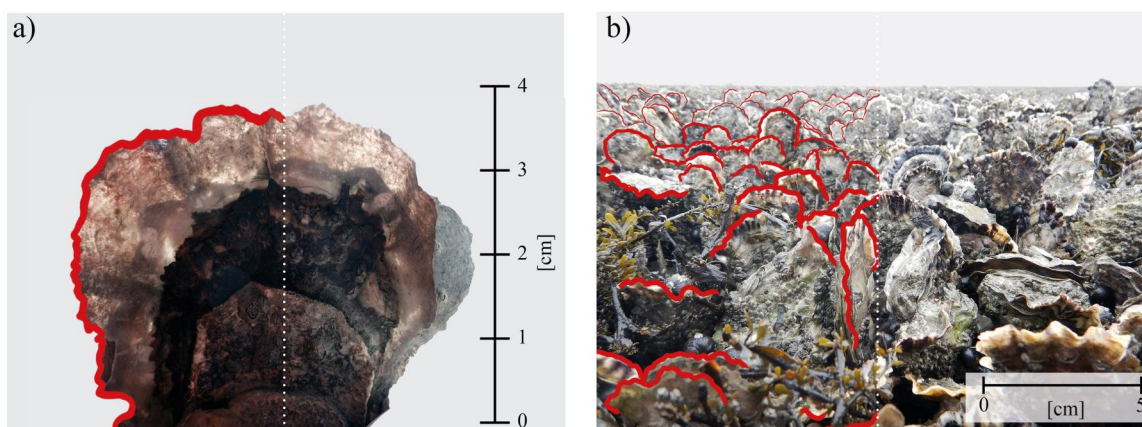
Figure 1. Photographs illustrating the sharp edges of the shells of (a) the top half of a *Magallana gigas* individual (courtesy of Senckenberg am Meer) and (b) a densely packed *M. gigas* reef surface recorded at Kaiserbalje in the German Wadden Sea (mean coordinates: 53.6470116°N, 008.2664760°E). Sharp shell edges are marked in red.

sequester carbon (Fodrie et al., 2017; Veenstra et al., 2021). However, compared to other marine ecosystems, like coral reefs, salt marshes, seagrass meadows, and mangroves, whose wave attenuating effects have been extensively studied, investigations quantifying wave attenuation and influencing hydro- and morphodynamic processes of oyster reefs remain sparse (Morris et al., 2018; Morris et al., 2021; Narayan et al., 2016; Walles, Mann, et al., 2015).

In shallow marine environments, oysters tend to form spatially extensive reef-like structures with complex, three-dimensional (3D) reliefs, resulting in an increased hydraulic bed roughness compared to the surrounding sea floor (Borsje et al., 2011; Gutiérrez et al., 2003; Hitzegrad, Brohmann et al., 2022; Markert, 2020). These ultra-rough surfaces can reach spatial extents up to several square kilometers (Bahr & Lanier, 1981; Folmer et al., 2017; Kennedy, 1996); examples of large-scale coverage are found in the central Wadden Sea between the Netherlands and Germany (Folmer et al., 2017; Reise et al., 2017) or the Korean Getbol (Choe et al., 2012; Choe & Kim, 2019; Kim & Ryu, 2020), while small-scale reefs, not directly addressed in this study are rather typical of the East coast of the USA. Individuals typically protrude from the surrounding sediment and form areas with high abundance in which individuals are densely packed and oriented vertically. The resulting ultra-rough surfaces are characterized by reef-wide attributes (e.g., the habitat morphology, abundance, and cluster formation), as well as the characteristics of the individual oysters (e.g., the species, shell shape, shell size, and shell orientation; Hitzegrad, Brohmann et al. (2022)). The two most common reef-building oyster species are the Pacific oyster *Magallana gigas* (Thunberg, 1793 formerly referred to as *Crassostrea gigas*) and the American oyster *Crassostrea virginica* (Gmelin, 1791), which inherit similar and differentiating morphological properties (Dame, 2016; Gosling, 2015; Hayward & Ryland, 2017). The shells of both species exhibit elongated, concentric shapes reaching lengths of 80–200 mm and widths of 50–100 mm. *M. gigas* individuals feature rugose and frilled surfaces. The shells of *M. gigas* are sculpted with about six bold raised ribs and glossy, crenulate shell edges. In contrast, *C. virginica* individuals feature smooth surfaces and shell edges. Both species, however, are sculpted with shell margins less than 1 mm in thickness forming razor-sharp edges (Figure 1) (García-March et al., 2007; Gosling, 2015; Hayward & Ryland, 2017; Nehring, 2011). The ultra-rough surfaces induce turbulence in the ambient flows, which causes vertical mixing within the water column and, thus, provides the filter-feeding oysters with more suspended organic matter and oxygen. Simultaneously, the ultra-rough surfaces reduce the energy flux of the ambient flow due to frictional energy dissipation (Nelson et al., 2004; Reidenbach et al., 2013; Wright et al., 1990). As the razor-sharp edges of individual oyster shells are a striking feature of oyster reefs, it is hypothesized that primarily the sharp edges function as nucleation for vortex separation of the ambient oscillating flows and, thus, are a key factor of the frictional wave energy dissipation.

The reef morphology and spatial extents of the reef structures depend on the seafloor morphology and the availability of hard substrate to settle on (Reise, 1998; Wehrmann et al., 2000; Wrange et al., 2010) and determine the wave energy transmission. When waves propagate over the reef structure, the incoming wave energy, E_i,
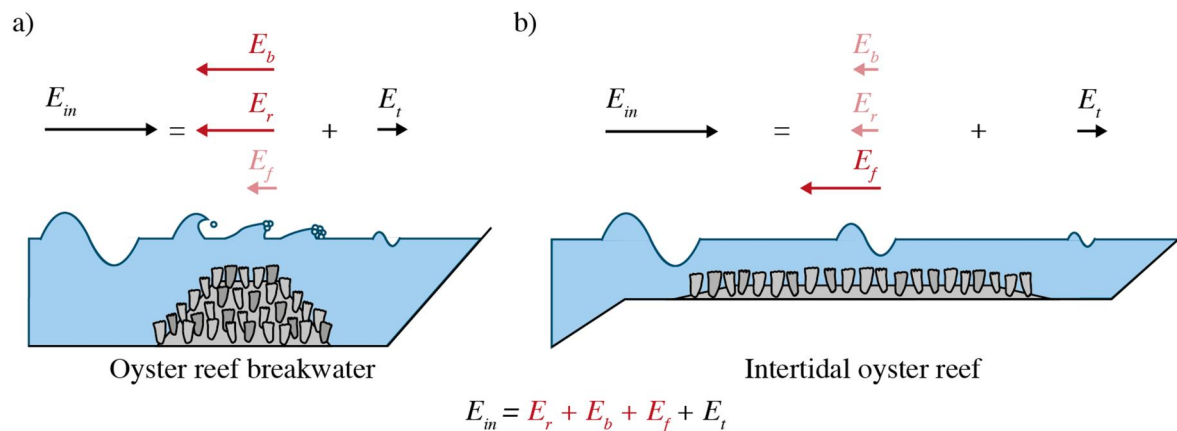
Figure 2. Schematic of the wave energy transmission over (a) a steep-edged oyster reef breakwater and (b) a shallow intertidal oyster reef, where E_{in} is the incoming wave energy, E_t the transmitted wave energy, E_r is the reflected wave energy, E_b is the wave energy dissipated due to wave breaking, and E_f is the wave energy dissipated due to frictional dissipation.

undergoes reduction due to reflection, dissipation due to wave breaking, and dissipation due to bed friction (Figure 2). The transmitted wave energy, E_t, is the remaining part of E_i after subtracting the reflected wave energy, E_r, the wave energy dissipated due to wave breaking, E_b, and the wave energy dissipated due to bed friction, E_f. The extent of these reductions (E_r, E_b, and E_f) depends on the relative height of the reef crest height in relation to the water depth and wave height (Chowdhury et al., 2019; Wiberg et al., 2019; Zhu et al., 2020). Moreover, the proportions of E_r and E_b are primarily governed by the seaward slope of the reef, increasing with a steeper slope. On the other hand, the proportion of E_f depends primarily on the bed surface characteristics, that is, the bed roughness and the interaction length of the reef surface with the waves. *C. virginica* reefs on the East Coast of the USA are, typically, narrow bathymetric features, with steep inclinations to a deeper oceanic section and narrow elevation surface grown over centuries (Morris et al., 2021; Ridge et al., 2017; Scyphers et al., 2011). Due to the abrupt water elevation changes, wave energy is reduced by a combination of reflection, dissipation by wave breaking, and, to a subordinate proportion, dissipation by bed friction (similar to conventional submerged wave breakers; e.g., van der Meer et al. (2005)). Incorporating these mechanisms, constructed reefs functioning as a nature-based solution (NbS) for coastal protection are often referred to as oyster reef breakwaters (Allen & Webb, 2011; Chowdhury et al., 2019; Ridge et al., 2017; Scyphers et al., 2011) (Figure 2a)). *M. gigas* has invaded the intertidal flats of the central Wadden Sea in Northern Europe as an invasive species over the last 20 years. In the process, formerly pristine and predominant blue mussel beds (*Mytilus edulis*), as the only available hard substrate for oyster larvae to settle on, have been transformed into oyster reefs (Folmer et al., 2017; Reise et al., 2017). Hence, *M. gigas* reefs in the central Wadden Sea are typically characterized by very shallow seabed slopes and large horizontal extents ($>km^2$) (Folmer et al., 2014, 2017; Markert, 2020; Reise et al., 2017). Due to the considerable interaction length of the reef surface with the waves, frictional dissipation is hypothesized to be the primary cause of wave energy decay, while breaking and reflection are secondary (Borsje et al., 2011; Walles, Salvador de Paiva, et al., 2015) (Figure 2b)); the second, shallow form of oyster coverage is explicitly addressed in this work.

Former studies focusing on wave-induced frictional dissipation and bed shear stress, τ_w, typically investigated bluntly-shaped roughness elements (i.e., sand grains: Kamphuis (1975), Jonsson (1966), You et al. (2009), Yuan and Madsen (2014); rippled beds: Brevik and Bjørn (1980) Mirfenderesk and Young (2003) or gravel beds: Sleath (1987), Dixen et al. (2008), Dunbar et al. (2023)), while few studies address frictional dissipation induced by sharp-edged roughness elements in oscillating flows. Mathisen and Madsen (1996) report on a wave flume study in which wave attenuation over triangular bars (bar height of 0.015 cm and bar spacing of 0.10 and 0.20 m) as a surrogate for a rippled bed has been investigated. For regular waves (wave periods $T_m = 2.59 \pm 0.28$ s and near-bed horizontal wave excursion amplitudes $a_b = 0.051 \pm 0.006$ m), they report wave friction factors $f_w = 0.31 \pm 0.06$ and $f_w = 0.19 \pm 0.02$ as well as hydraulic roughness lengths $k_w = 0.213 \pm 0.037$ m and $k_w = 0.111 \pm 0.032$ cm for 0.1 and 0.2 m bar spacing, respectively. Mirfenderesk and Young (2003) investigated waves over similar triangular bars (bar height of 0.0136 m and bar spacing of 0.065 m) and report $f_w = 1.0$–0.21

for monochromatic waves (T = 2.0 s) with varying a_b = 0.015–0.164 m and near-bed maximum velocity amplitudes $u_{b,max}$ = 0.05–0.51 m/s, while assuming a fixed k_w = 0.05 m.

Ultra-rough surfaces have been extensively studied as analogies to submerged canopies in various flow scenarios, for example, air flow over and through urban areas (Britter & Hanna, 2003; Ramponi et al., 2015) and vegetation (Belcher et al., 2012; Finnigan, 2000; Raupach & Shaw, 1982), as well as water flow (unidirectional (Conde-Frias et al., 2023; He et al., 2022; Monti et al., 2022; Nepf & Vivoni, 2000) and oscillating (Abdolahpour et al., 2017; Buckley et al., 2022; Lowe, 2005; Van Rooijen et al., 2020, 2022) over and through aquatic vegetation and coral reefs. Canopy flow models conceptually represented rough surfaces by three-dimensional arrangements of vertical roughness elements of various spacing. When subjected to oscillating flow, the roughness elements induce a frictional resistance due to the sum of the drag and inertia forces, as described by the Morrison equation (Dean & Dalrymple, 1991). Consequently, the flow resistance induces a gradient between the spatially-averaged in-canopy flow velocities and the unaffected free-stream velocity above the canopy forming a mixing or boundary layer (depending on the density of roughness elements), giving rise to turbulence production and wave energy dissipation.

Frictional dissipation induced by oyster reefs has, thus far, only been investigated in detail for *C. virginica* reefs subjected to unidirectional flows. Several studies report maximum current-induced bed shear stresses of τ_c = 0.4 – 4.0 N/m^2 near the edges of the oysters (Kitsikoudis et al., 2020; Reidenbach et al., 2013; Whitman & Reidenbach, 2012). Kitsikoudis et al. (2020) conclude that their estimated drag coefficients of oyster reefs (C_D = 0.31) are lower than those of mangroves pneumatophores (C_D = 0.26 ± 0.15; Norris et al. (2019)) and higher than those of coral reefs (C_D = 0.009–0.015; Reidenbach et al. (2006)). As a further ultra-rough oceanic surface, shallow-water coral reefs are known to attenuate wave energy and have been thoroughly studied regarding frictional dissipation (Harris et al., 2018; Huang et al., 2012; Lowe & Falter, 2015). Typical wave friction factors found in past studies are in the range of f_w = 0.1–0.4 (Harris et al., 2018; Lowe et al., 2005; Monismith et al., 2013; Nelson, 1996), while Monismith et al. (2015) report even higher f_w = 1.80 ± 0.07, due to the complex surface structure found in their field study. Donker report f_w = 0.11–0.22 for an intertidal mussel bed and Paul and Amos (2011) report f_w = 0.02–0.08 for a seagrass meadow. Despite the lacking knowledge of the wave-induced frictional dissipation, the potential of the ultra-rough surfaces of oyster reefs for reducing wave energy as a NbS in coastal protection has been addressed in several studies (Chowdhury et al., 2019; Jiang et al., 2022; Manis et al., 2015; Wiberg et al., 2019; Zhu et al., 2020), especially for *C. virginica* reefs. Transmission coefficients, K_t, that is, a measure of the remaining energy of a sea state after a specific propagation distance, have been reported for natural and restored *C. virginica* reefs ranging between K_T = 0.19–0.50, strongly depending on the reef crest elevation in relation to the water depth and the wave height (Garvis, 2012; Lunt et al., 2017; Manis et al., 2015; Wiberg et al., 2019; Zhu et al., 2020). Based on a field study on 15 *C. virginica* reefs designed to function as breakwaters along the East Coast of the USA, Morris et al. (2021) conclude that these are often ineffective at attenuating waves. The authors call for more research pertaining to reef characteristics, especially considering larger reef widths, implying increased bed friction by increasing the interaction length between waves and reef surface. Despite the general knowledge of *M. gigas* reefs' potential in Northern Europe to dissipate wave energy (Bouma et al., 2014), only one study by Borsje et al. (2011) has specifically described their impact on wave attenuation. The authors report on a flume experiment in which an *M. gigas* reef yields roughly 30% stronger wave height reduction than a blue mussel bed (*M. edulis*; both 3.10 m long. Although these studies have contributed to a better understanding of wave energy attenuation by oyster reefs, a comprehensive understanding of the underlying mechanisms, especially the influence of the bed friction induced by ultra-rough surfaces, is still lacking.

Based on the knowledge gaps mentioned above, the overall objective of this work is to systematically investigate the influence of ultra-rough geometries as surrogates for ultra-rough oceanic surfaces, for example, oyster shells, on frictional wave energy dissipation. More specifically, this study aims to investigate the following specific objectives.

- to investigate the influence of sharp edges of roughness elements, as well as the spacings between roughness elements on frictional energy dissipation,
- to quantify the influence of varying near-bed horizontal wave excursion amplitudes, a_b, in relation to the spacing between roughness elements, λ, on the frictional energy dissipation, and
- to compare different determination methods of frictional energy dissipation in oscillating flows.

In a comprehensive laboratory study, primitive surrogate models of large roughness elements, with varying shapes and spacing between elements, have been used to approximate ultra-rough surfaces of oyster reefs and are subjected to regular waves to investigate the influence of their edginess and density. Wave energy dissipation will be evaluated by comparing water surface level elevation and flow velocity measurements.

2. Materials and Methods

2.1. Experimental Setup

The experimental facility employed in this study is a wave flume at Leichtweiß-Institute for Hydraulic Engineering and Water Resources, Technische Universität Braunschweig, Braunschweig, Germany. It is 90 m long, 1.0 m wide, and 1.3 m high (Figure 3a). The flume is equipped with a piston-type wave generator and a passive wave absorber. The bed surface surrogates investigated in this work are positioned at $x = 35$ m, each with a length of 16 m. The tested roughness elements were mounted to marine plywood panels installed on the flume bottom, having a height of 0.04 m. The height difference between the plywood panels and the bottom of the flume was transitioned by a uniform slope (1:10) with a length of 0.4 m in front and behind the test section.

This work focuses on understanding the effects of ultra-rough oceanic surfaces through surrogate modeling; conceptually, natural roughness is approximated by primitive two-dimensional (2D) shapes, such as semicircles and squares, combined with different distances at a geometric scale of 1:3. Figure 3b shows the three primitive combinations used in this work to construct six bed surface surrogates, which were then exposed to surface gravity waves. These primitive combinations are labeled *semicircle*, *lamella* (a distorted square), and *mix* (combinations thereof), which were examined, with two distinct spacings between the roughness elements (Figure 3c). The *semicircle* shape was selected as a widely used surrogate model for very rough oceanic surfaces, for example, rippled beds (Brevik & Bjørn, 1980; Coleman et al., 2008; Mathisen & Madsen, 1996; Mirfenderesk & Young, 2003). With the *lamella* shape, the sharp margins of the oyster shells should be depicted in isolation. The *mix* shape was selected as a primitive representation of the entire oyster, including the sharp shell margin and the body below. Thus, the *lamella* and the *mix* shape represent ultra-rough oceanic surfaces as defined in the introduction. The *semicircle* type was made of halved wooden palisades with a radius of 0.05 m. To prevent swelling, treated wood was used. Cracks and irregularities in the surfaces were mended with silicone. The *lamella* type consists of aluminum sheets with a thickness of 1.0 mm and a height of 0.05 m. For the *mix* type, identical wooden palisades as for the *semicircle* were cut to a height of 0.04 m and sculpted with an aluminum sheet of 0.01 m height, resulting in a total height of 0.05 m. Hence, all surrogate surfaces have a total roughness height $k_t = 0.05$ m, measured from the bottom to the maximum elevation of the roughness element (peak-to-trough roughness height (Chung et al., 2021)). On prototype scale, $k_{t,prototype} = 0.15$ m is similar to measured heights of protruding oyster shells (∼0.10–0.15 m) (Hitzegrad, Brohmann et al., 2022; Kitsikoudis et al., 2020; Manis et al., 2015). The total length of the surrogate surfaces of 16.0 m reflects 48.0 m in prototype scale, which is in the same order of magnitude as the widths of intertidal oyster reefs in the central Wadden Sea (Folmer et al., 2017; Hitzegrad, Brohmann et al., 2022; Reise et al., 2017). Furthermore, all surrogate surfaces exhibit a uniform distribution in the lateral direction of the flume to further simplify the complex, three-dimensional oyster reef surfaces. Two center-to-center spacings of the roughness elements $\lambda_1 = 0.10$ m and $\lambda_2 = 0.20$ m were investigated, and the configurations are denoted as *1* or *2*, respectively. The small spacing was chosen according to the diameter of the *semicircle* types. The spacing configurations led to a total of 80 roughness elements for the dense configurations (5 elements/m) and 40 for the sparse configurations (2.5 elements/m). Hence, a total of six bed surface surrogate configurations (*semicircle 1 (SC1)*, *semicircle 2 (SC2)*, *mix 1 (M1)*, *mix 2 (M2)*, *lamella 1 (L1)*, and *lamella 2 (L2)*), as well as an additional *reference* surface (*REF*), without roughness elements, were tested. Hereof, the four configurations *L1*, *L2*, *M1*, and *M2* feature sharp-edged roughness elements (hereinafter referred to as sharp-edged surfaces) as surrogates of ultra-rough oceanic surfaces, for example, oyster reefs, and the two configurations *SC1* and *SC2* feature bluntly-shaped roughness elements (hereinafter referred to as bluntly-shaped surfaces) as surrogates of widely investigated very rough surfaces. It should be noted that this distinction is based on the topographical characteristics and not the induced flow regimes, which are discussed in Section 3.3.

Regular surface gravity waves were generated with a constant mean wave height of $H_m = 0.147$ m at WG_4 and varying mean wave periods of $T_m = 1.5$ s; 2.0 s; 2.5 s; 3.0 s (see Table 1). The incoming wave height is defined as $H_{m,in} = H_{WG4}$ as the first WG on the tested bed surfaces ($x_{WG4} = 36.0$ m). The water depth was kept constant at $d = 0.70$ m. The relative water depth d/L, where L is the wave length, corresponds to the transitional zone in all
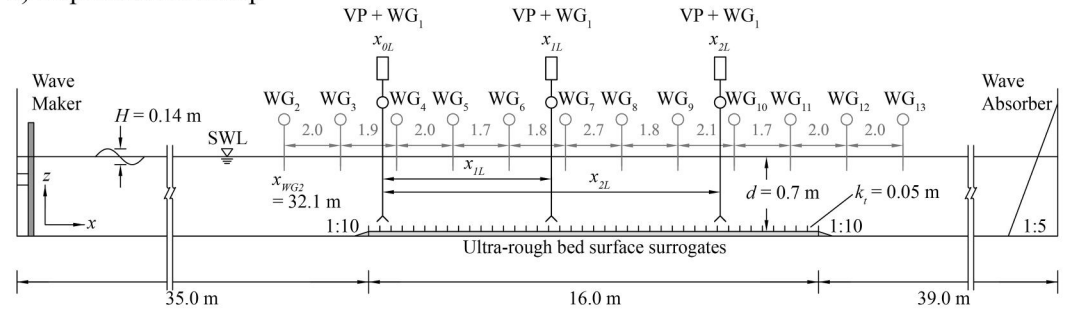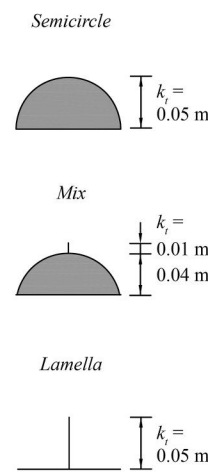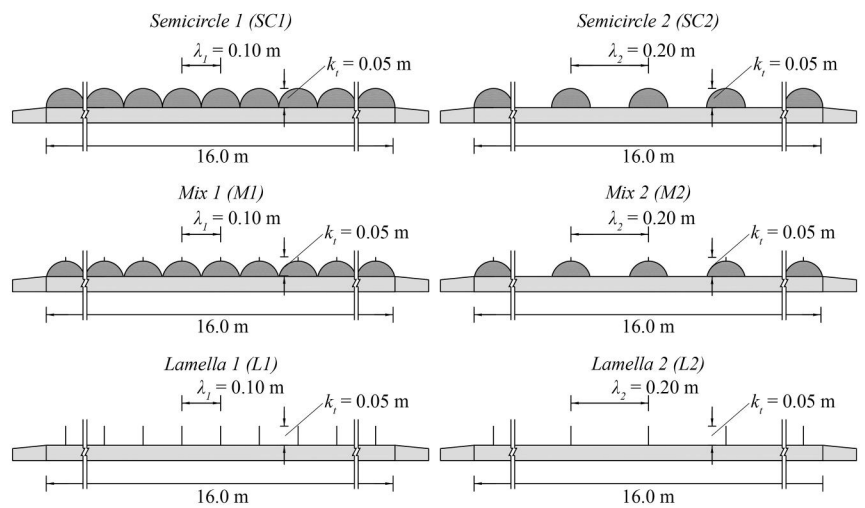
Figure 3. Schematic of (a) the experimental setup in the wave flume (not to scale), where SWL is still water level, and k_t is the total roughness height. Positions of the Vectrino Profiler (VP) and Wave Gauge 1 (WG_1) are listed in Table 2; (b) side-views of the primitive combinations; and (c) of the six tested bed surface configurations: *semicircle 1 (SC1)*, *semicircle 2 (SC2)*, *mix 1 (M1)*, *mix 2 (M2)*, *lamella 1 (L1)*, and *lamella 2 (L2)*. (d) Photographs of the experimental setup with *SC1*, *M1*, and *L1*.

Table 1
Surface Gravity Wave Parameters

d [m]	H_m [m]	T_m [s]	L [m]	d/L [-]	H_m/L [-]	u_b [m/s]	a_b [m]	Re [-]	KC [-]	λ_1/a_b [-]	λ_2/a_b [-]
0.7	0.147	1.5	3.10	0.23	0.05	0.16	0.04	$5.47 \cdot 10^3$	4.5	2.5	5.0
		2.0	4.67	0.15	0.03	0.21	0.07	$1.26 \cdot 10^4$	8.1	1.4	2.9
		2.5	6.15	0.11	0.02	0.24	0.09	$1.66 \cdot 10^4$	11.3	1.1	2.2
		3.0	7.57	0.09	0.02	0.25	0.12	$2.46 \cdot 10^4$	14.3	0.8	1.7

Note. d is the water level, H_m is the mean wave height, T_m is the wave period, L is the wave length, d/L is the relative water depth, H_m/L is the wave steepness, u_b is the maximum near-bed wave orbital horizontal velocity amplitude, a_b is the maximum near-bed horizontal wave excursion amplitude, Re is the Reynolds number, KC is the Keulegan-Carpenter number, and λ_1/a_b and λ_2/a_b are the relative spacings between roughness elements depending on bed surface configuration.

four hydrodynamic cases (d/L = 0.09–0.23). Wave steepness H_m/L varied between 0.02 and 0.05. The second-order Stokes wave theory is the best fit for all hydrodynamic conditions (Le Méhauté, 1976). Wave conditions were selected to cover a wide range of near-bed maximum velocity amplitudes, $u_{b,max}$, while avoiding wave-breaking (H/L < 0.143); thereby, wave energy dissipation is caused by frictional dissipation only. The wave-boundary-layer Reynolds numbers, Re, range from Re = $5.47 \cdot 10^3$–$2.46 \cdot 10^4$. Here, Re is defined as:

$$Re = \frac{a_b^2 \cdot \omega}{\nu},$$ (1)

where a_b is the near-bed horizontal excursion amplitude directly at the bed surface, $\omega = T_m/(2\pi)$ is the angular frequency, and $\nu = 1.2254 \cdot 10^{-6}$ m²/s is the kinematic viscosity. Based on the flow criteria suggested by Kamphuis (1975) for wave bottom boundary layers, it is expected that the boundary layers are in transitional to rough turbulent regime, when assuming that the relative roughness, a_b/k_w (where k_w is the hydraulic roughness length) is similar to a relative roughness when applying the total roughness height a_b/k_t. The Keulegan-Carpenter numbers, KC, are defined as:

$$KC = \frac{u_b \cdot T_m}{k_t}.$$ (2)

The relatively large KC = 4.5–14.3 indicate that vortex shedding may occur, which could lead to complex flow patterns. The hydrodynamic conditions reflect realistic conditions in the German Wadden Sea considering a Froude scaling of 1:3, with a prototype water depth of $d_{prototype}$ = 2.10 m, a prototype mean wave height of $H_{m,prototype}$ = 0.44 m, and prototype mean wave periods $T_{m,prototype}$ between 2.6 and 5.2 s. The water depth $d_{prototype}$ represents high tide conditions over the vertical growth ceiling of oyster reefs at 50%–60% aerial exposure time (Ridge et al., 2017; Rodriguez et al., 2014). Hence, the experimental conditions depict deeply submerged roughness elements with d/k_t = 14. The relative spacings, defined as the ratio between the spacing between roughness elements λ and a_b vary between λ/a_b = 0.8–5.0.

The water surface elevation η was measured with 13 resistive wave gauges (WG, in-house manufactured) at a sampling frequency of 60 Hz. The WGs were calibrated to an accuracy of >99%. Wave gauges $WG_2 - WG_{13}$ were positioned at fixed locations along the flume (Figure 3). Velocity profiles were recorded at several horizontal positions depending on multiples of the theoretical wave length (x_{0L}, x_{1L}, x_{2L}, and x_{5L}; see Table 2). A Nortek Vectrino Profiler (VP; software version 1.32.2779) was jointly placed with wave gauge WG_1 to simultaneously record velocity profiles and water surface level elevations at each position. The VP was used to capture the instantaneous velocity components in the x-, y-, and z-direction, termed u_i, v_i, and w_i, respectively, following the coordinate system in Figure 3. The velocity components were recorded at a sampling frequency of 100 Hz and an

Table 2
Positions of the Vectrino Profiler (VP) and Wave Gauge 1 (WG_1), Depending on the Tested Hydrodynamic Case (Mean Wave Period T_m and Near-Bed Horizontal Wave Excursion Amplitudes a_b)

T_m [s]	a_b [m]	x_{0L} [m]	x_{1L} [m]	x_{2L} [m]	x_{5L} [m]	N [-]
1.5	0.04	35.5	–	42.0	51.0	25
2.0	0.07	35.5	40.2	44.7	–	17
2.5	0.09	35.5	42.0	47.6	–	13
3.0	0.12	35.5	43.0	50.5	–	10

Note. N is the number of evaluated wave cycles.

accuracy of ±1 mm/s. The bin size of the VP was set to 1 mm, and 20 bins (and partially 30 bins) were selected, centered around the "sweet spot" of the measuring range, resulting in a profiling range of 20 mm, or 30 mm, per recording to assure validity similar to, for example, Koca et al. (2017). Glass micro spheres (diameter of 10 μm) were used as seeding material for the VP measurements. The signals of the VP and the WGs were synchronized using a trigger signal. The exact horizontal positions were slightly adjusted (±0.05 m) from the theoretical value to record the velocity profiles above the highest point of a roughness element. Repeated experiments were carried out with adjusted vertical positioning of the VP by $\Delta z = 0.02$ m until the wave bottom boundary layer was recorded completely. The thickness of the wave bottom boundary layer δ was determined visually, ranging between 4 and 14 mm from the peak of the roughness elements, depending on the structural configuration and the hydrodynamic cases (see Section 3.2). A total of 479 runs with durations of 120 s were recorded. The analyzed time series were trimmed, beginning with the first time instance at which the surface level elevation $\eta = 0.7 \cdot H_m$. The number of analyzed wave cycles, N, varies between 10 and 25 depending on the time span before reflected waves reach the measurement section, calculated according to the Stokes second-order wave theory. The time spans are limited intentionally to exclude interactions between the incoming and the reflected waves, which potentially influence the flow characteristics near the bed surfaces. Furthermore, over more extended time spans, the wave drift, resulting in a net discharge of water near the free surface in the direction of the waves, would introduce a return flow near the bed surface, causing an additional streaming effect (Fredsøe et al., 1999; Sumer & Fuhrman, 2020). The original data set can be accessed through Hitzegrad, Köster, et al. (2022).

2.2. Data Processing

The water surface elevation data were filtered by applying a Butterworth lowpass filter with a cutoff frequency of 10 Hz (Butterworth, 1930). Next, a zero-down crossing was conducted to determine the wave parameters in the time domain, including H_m, and T_m (Gormus, 2021).

The instantaneous velocity data were filtered by removing data with low signal-to-noise ratios ($SNR < 30$ dB) and low correlation ($COR < 70\%$) (Raushan et al., 2020). Applying these filters predominantly caused distal bins from the sweet spot of the VP to be removed from the data, resulting in a reduced number of analyzed bins to an average of 18 ± 3, which is in agreement with the recommended 18 bins by Thomas et al. (2017). Further, the phase-space method by Goring and Nikora (2002) was applied to despike the data and exclude outliers. The deleted data was replaced by interpolation with a third-order polynomial.

2.3. Quantification of Frictional Wave Energy Dissipation

The frictional energy dissipation of wave energy is commonly parameterized by the hydraulic roughness length, k_w, the wave-induced bed shear stress, τ_w, and the wave friction factor, f_w. Several methods have been presented in the literature to determine the wave-induced bed shear stress, τ_w, and to quantify the hydraulic roughness. Typically, k_w is defined as the equivalent sand roughness (Nikuradse, 1933). Jonsson (1966) introduced the wave friction factor f_w as a dimensionless parameter that links τ_w to the near-bed wave orbital horizontal velocity amplitude u_b:

$$\tau_w = \frac{1}{2} \cdot \rho \cdot f_w \cdot u_b^2, \tag{3}$$

where ρ is the density of water.

Bed shear stress can be (a) measured directly using a bed shear plate (Kamphuis, 1975; Mirfenderesk & Young, 2003); (b) derived from instantaneous velocity measures within the bottom boundary layer by evaluating the log-profile (Soulsby, 1983), the Reynolds stress (Sleath, 1987; Thompson et al., 2012), the turbulent kinetic energy (TKE) (Bagherimiyab & Lemmin, 2013; Dade et al., 2001; Soulsby, 1983; Thompson et al., 2012; Zhang et al., 2020), or the inertial dissipation (Stapleton & Huntley, 1995; Thompson et al., 2012); or, (c) from the attenuation of wave energy over the length of the bed surface by establishing an energy balance (EB) and application of empirical relationships as found by Jonsson (1966), Swart (1974), Kamphuis (1975), Kajiura (1968), Nielsen (1992), Soulsby (1997), or Sumer and Fuhrman (2020).

This work uses the EB method to derive τ_w from the measured surface elevations using Swart's relationship (1974) with Sumer and Fuhrman's adaptation (2020) as the most recent and one of the most widely used

approaches in field studies (Donker et al., 2013; Lacy & MacVean, 2016; Lentz et al., 2016; Lowe et al., 2005; Monismith et al., 2015; Paul & Amos, 2011; Rogers et al., 2016; Thompson et al., 2012), and wave channels (Brevik & Bjørn, 1980; Mirfenderesk & Young, 2003; Simons et al., 1993; Yao et al., 2020). The TKE method, according to Thompson et al. (2012), is applied to derive τ_w from the instantaneous velocity data measured at a single location, as it has been declared the most accurate in previous literature (Kim et al., 2000; Thompson et al., 2012; Zhang et al., 2020).

2.3.1. Energy Balance (EB) Method

The EB method determines the maximum wave-induced bed shear stress, $\tau_{w,max}$, by assuming that two major effects dissipate wave energy in shallow marine environments: wave breaking, parametrized by the wave breaking dissipation rate, e_b (Battjes & Janssen, 1978; Thornton & Guza, 1983), or bed friction, parametrized by the frictional dissipation rate, e_f (Ardhuin et al., 2001; Young & Gorman, 1995). The proportions of both effects depend on the slope and the surface characteristics of the bed. An energy balance was used that includes energy flux losses ΔF of both effects:

$$\frac{\Delta F}{\Delta x} = \frac{\Delta(E \cdot c_g)}{\Delta x} = -e_f - e_b, \tag{4}$$

where E is the total wave energy, c_g is the group velocity, and Δx is the interaction length of the waves with the bed surface. The total wave energy for second-order Stokes waves is determined following Dong et al. (2020):

$$E = \frac{1}{8} \cdot \rho \cdot g \cdot H^2 \cdot \left(1 + \left(\frac{H \cdot k}{2}\right)^2 \cdot \left(\frac{5}{8} + \frac{52 \cdot (sinh(k \cdot d)^4 + 36 \cdot (sinh(k \cdot d)^2 + 9))}{32 \cdot (sinh(k \cdot d)^4)}\right)\right), \tag{5}$$

where $k = 2\pi/L$ is the wave number. In this work, Δx was defined by the distance between WG_4 and WG_{11} to $\Delta x = x_{WG11} - x_{WG4} = 49.8–36.0$ m $= 13.8$ m, covering most of the length of the tested surrogate surfaces, as shown in Section 2.1. The group velocity c_g was calculated according to the second-order Stokes wave theory (Le Méhauté, 1976). The hydrodynamic cases were chosen so that no wave breaking occurred, thus $e_b = 0$. Therefore, as defined in Equation 4, the energy dissipation only results from bed friction e_f. Next, e_f was linked to the energy dissipation factor, f_e, following Jonsson (1966):

$$e_f = \frac{2}{3\pi} \cdot f_e \cdot u_{b,max}^3, \tag{6}$$

where f_e is the energy dissipation factor and $u_{b,max}$ is the maximum near-bed orbital velocity amplitude directly above the wave bottom boundary layer δ. According to Madsen (1994) and Mathisen and Madsen (1996), for large relative roughness $k_w/a_b > 0.1$, which is assumed here, f_e is related to f_w by the phase angle, ϕ, between the near-bed orbital velocity u_b and the bed shear stress τ_w:

$$f_e = f_w \cdot cos(\phi), \text{with} \tag{7}$$

$$\phi = 33 - 6 \cdot \log\left(\frac{u_b}{k_w \cdot \omega}\right) \text{ for turbulent flow conditions, and} \tag{8a}$$

$$\phi = 45° \qquad \text{for laminar flow conditions.} \tag{8b}$$

Based on the Reynolds numbers Re and the relative roughness a_b/k_w, it is assumed that the boundary layer is either in the transitional or turbulent regime (compare Section 2.1). Therefore, to determine the relationship between f_w and k_w, the following expression by Sumer and Fuhrman (2020) was applied to determine the relationship, which is valid for laminar, transitional and rough turbulent regimes:

$$f_w = f_{w,s} + (f_{w,r} - f_{w,s}) \cdot \left(1 - \exp\left(-\frac{\sqrt{f_w/2}}{10} \cdot \frac{Re}{a_b/k_w}\right)\right)^3, \tag{9}$$

where $f_{w,s}$ is the wave friction factor for a smooth wave bottom boundary layer according to Fredsøe and Deigaard ([1992](#)) and $f_{w,r}$ is the wave friction factor for a rough wave bottom boundary layer as developed by Swart ([1974](#)) and adapted by Nielsen ([1992](#)) and Fuhrman et al. ([2013](#)) for fully developed rough turbulent flows:

$$f_{w,s} = 0.035 \cdot Re^{-0.16}, \text{and}$$

(10)

$$f_{w,r} = \exp\left(5.5 \cdot \left(\frac{k_w}{a_b}\right)^{0.2} - 6.7\right)$$

(11)

In this work, f_w and k_w were determined iteratively, with the total roughness height $k_t = 0.05$ m as the initial input value for k_w. Finally, $\tau_{w,max}$ was determined as follows:

$$\tau_{w,max} = \frac{1}{2} \cdot \rho \cdot f_w \cdot u_{b,max}^2.$$

(12)

In wave flumes, the total wave attenuation, and thus, the energy flux losses ΔF, include secondary effects due to sidewall friction and other imperfections of the flume (Brevik & Bjørn, [1980](#); Hunt, [1952](#); Mirfenderesk & Young, [2003](#)). To eliminate these model effects, the wave height reductions that also arose in the *REF* cases were subtracted for each tested bed surface configuration (for the hydrodynamic cases with $a_b = 0.04$ m; 0.07 m; 0.09 m; 0.12 m: 8%, 5%, 5%, and 0% of K_T between WG_4 and WG_{11}, respectively). Hence, removing these model effects ensured only analyzing the wave attenuation due to bed friction.

2.3.2. Turbulent Kinetic Energy (TKE) Method

The maximum bed shear stress $\tau_{w,max}$ was also determined from the measured instantaneous velocity components, u_i, v_i, and w_i, by applying the TKE method. To that end, a Reynolds decomposition for turbulent flow conditions was applied to the instantaneous velocity components, for example, for u_i in the stream-wise direction:

$$u_i = \overline{u} + \tilde{u} + u',$$

(13)

where $\overline{u}$ is the time-averaged velocity component, $\tilde{u}$ is the wave-related component, and u' is the turbulent fluctuation. The ensemble-averaged component $\langle u \rangle = \overline{u} + \tilde{u}$ has been calculated following a conditional averaging method (Petti & Longo, [2001](#); van der A et al., [2017](#); van der Zanden et al., [2018](#)):

$$\langle u \rangle = \frac{1}{N} \sum_{n=0}^{N-1} u(t + t_n) \quad 0 \leq t < T,$$

(14)

where t is the time increment, and t_n is the cycle trigger, defined as the time instant of the nth zero-up crossing of the water surface measured at WG_1. The turbulent component is then calculated by:

$$u'(t) = u_i(t) - \langle u(t) \rangle.$$

(15)

The time-averaged velocities are determined by:

$$\overline{u} = \frac{1}{T} \int_0^T \langle u \rangle dt$$

(16)

and subsequently subtracted from $\langle u(t) \rangle$ to obtain the wave-related velocity component $\tilde{u}$, that is, the phase-averaged orbital velocities.

The lateral and bottom-normal turbulent velocity components, v' and w', have been decomposed similarly. The turbulent kinetic energy, *TKE* (per mass unit) is then calculated according to Soulsby ([1981](#)) and ([1983](#)):

$$TKE = \frac{1}{2} \cdot \left(\overline{u'^2} + \overline{v'^2} + \overline{w'^2} \right). \tag{17}$$

A short sensitivity analysis has shown that the time series adequately depict the phase-averaged velocities and the maximum near-bed turbulent kinetic energy $TKE_{max,b}$ (see Figure A1). The maximum bed shear stress is calculated as follows:

$$\tau_{w,max} = C \cdot \rho \cdot TKE_{b,max}, \tag{18}$$

where $TKE_{b,max}$ is the maximum near-bed turbulent kinetic energy, and C is an empirical coefficient introduced by Soulsby (1981). A correlation factor of $C = 0.19$ has been found to apply to various flow conditions and bed surfaces (e.g., flat, rippled, and vegetated) but has mainly been utilized for unidirectional flows (Biron et al., 2004; Pope et al., 2006; Stapleton & Huntley, 1995; Thompson et al., 2012). The parameters f_w and k_w have been determined by rearranging Equations 9 and 12.

3. Results

First, this section presents the evolution of the wave height and the near-bed velocity as the waves propagate over the different surfaces. Dependent parameters, such as the wave friction factor, the bed shear stress, and the hydraulic roughness length, are investigated with foci on the different determination methods and the general effect of the sharp edges.

3.1. Evolution of the Wave Height

The evolution of the normalized mean wave heights, $H_m/H_{m,in}$, over the length of the structures, x/L (Figure 4; values listed in Table C1), reveals distinct influences of the different bed surface surrogate configurations on the wave progression. Here, the incoming wave height is defined as $H_{m,in} = H_{WG4}$ as the first WG on the tested bed surfaces ($x_{WG4} = 36.0$ m). WG_7 has been deleted from the analysis due to measurement errors. The evolution of $H_m/H_{m,in}$ exhibits a gradual decline over the length of the test section for all cases and configurations, with standard deviations of less than 1% between repetitions (gray areas in Figure 4).

The bluntly-shaped surfaces, *SC1* and *SC2*, show a minor overall wave height reduction of 1%–2%, with a slightly more significant reduction of 5% for the case of *SC2* with $a_b = 0.12$ m. The *mix*-type surfaces cause more substantial wave height reductions of 6%–12% for *M1* and 6%–15% for *M2*. The most substantial reductions can be observed for the *lamella*-type surfaces, with 8%–16% for *L1* and 16%–24% for *L2*. The configurations with large spacing λ_2 between roughness elements (*L2*, *M2*, and *SC2*) cause more pronounced wave height reductions than those with small spacing λ_1 (*L1*, *M1*, and *SC1*) when comparing the configurations with the same roughness elements with different spacings (e.g., 8%–16% for *L1* and 16%–24% for *L2*).

The sharp-edged surfaces (*L2*, *L1*, *M2*, and *M1*) cause significantly higher wave height reductions for all hydrodynamic cases compared to the bluntly-shaped surfaces. This trend indicates a clear contribution of the sharp edges of the roughness elements on the wave energy dissipation. The shape of the roughness element below the edge exerts a subordinate influence, as the *semicircle*-type surfaces barely influence the wave height reduction.

Considering the hydrodynamic cases, the most considerable wave height reductions can be observed for the tested mid-range near-bed horizontal wave excursion amplitudes $a_b = 0.07$ and 0.09 m. In comparison, wave height reductions are less pronounced for the small ($a_b = 0.04$ m) and the large ($a_b = 0.12$ m) near-bed horizontal wave excursion amplitude. This trend is consistent for all bed surface configurations. Hence, for this experimental setup, waves with a_b slightly below the spacing of roughness elements λ are most influenced by the rough bed surface.

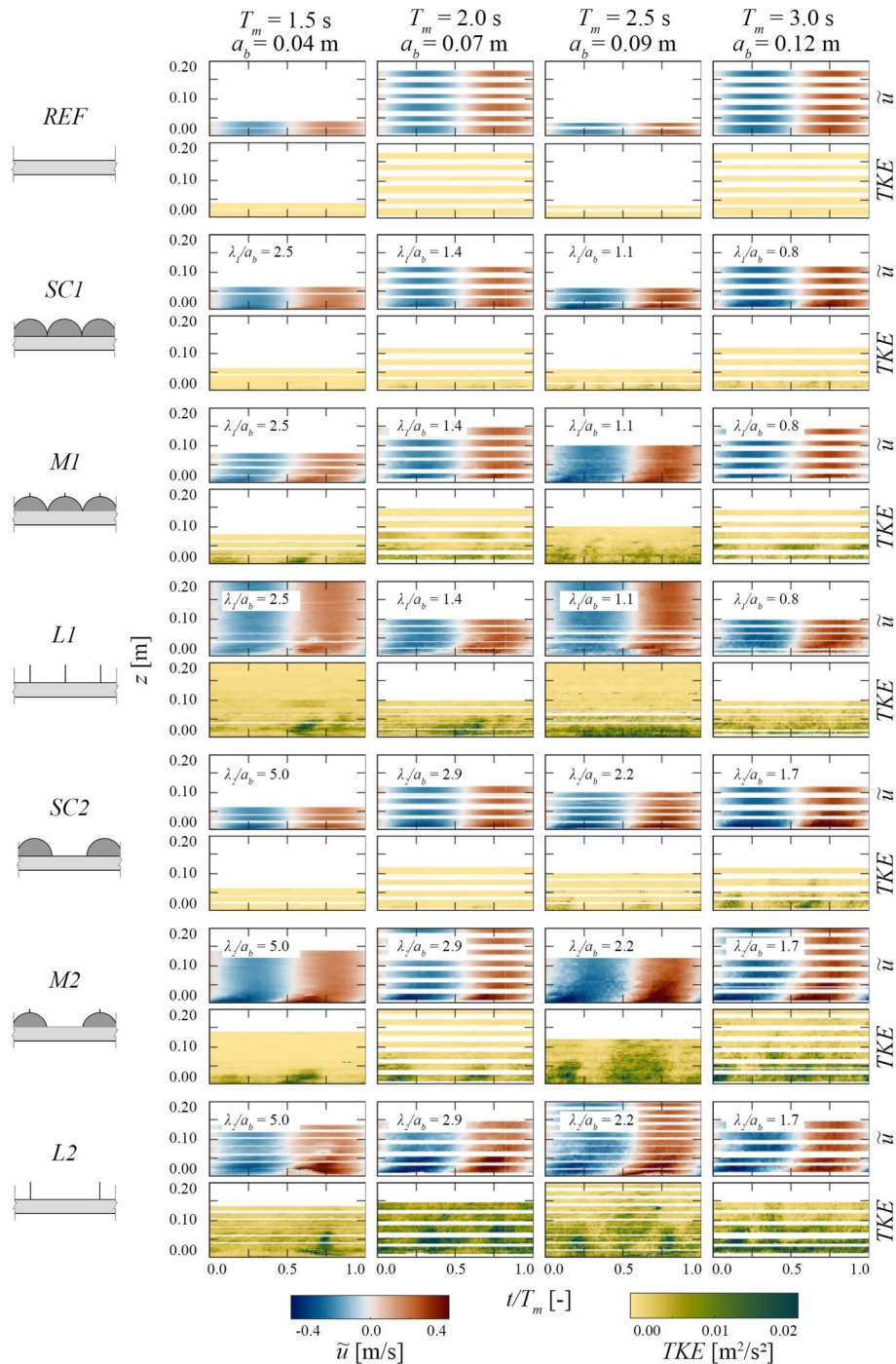### 3.2. Near-Bed Horizontal Velocity and Turbulent Kinetic Energy

The vertical and temporal distributions of the phase-averaged horizontal orbital velocities $\tilde{u}$ and the turbulent kinetic energy *TKE* (Figure 5, and Figure B1, based on Equations 13–18) further illustrate differences between the tested bed surfaces. Applying a zero-down crossing method, first, the development of $\tilde{u}$ and *TKE* under the wave
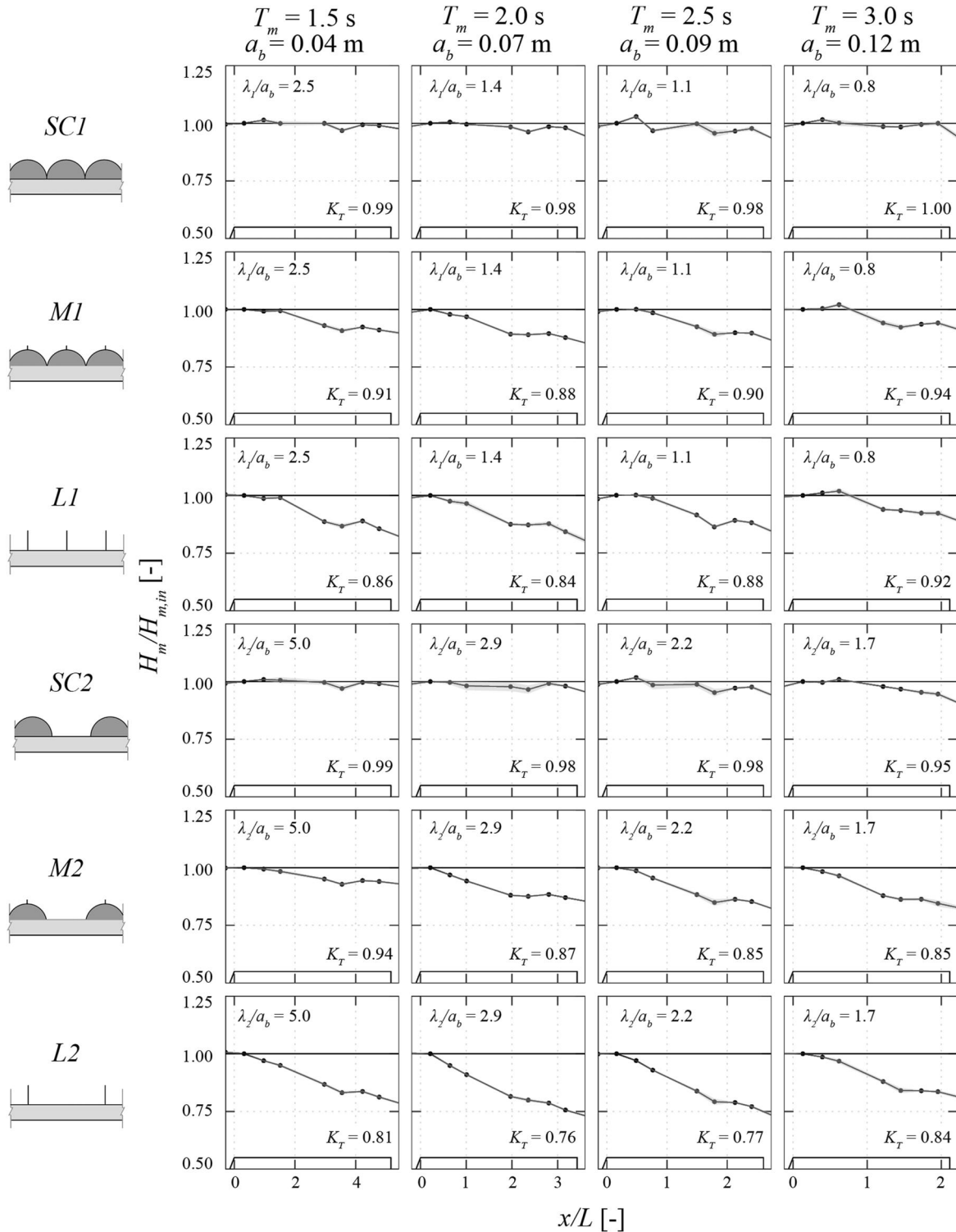
Figure 4. Evolution of the normalized mean wave heights $H_m/H_{m,in}$ [-] over the dimensionless length of the surrogate surfaces divided by the wave length x/L. The incoming wave height $H_{m,in} = H_{m,WG4}$ at $x = 36.0$ m. Records are sorted by bed surface configurations (*SC1*: *semicircle 1*, *M1*: *mix 1*, *L1*: *lamella 1*, *SC2*: *semicircle 2*, *M2*: *mix 2*, *L2*: *lamella 2*) and hydrodynamic cases (mean wave period T_m and near-bed horizontal wave excursion amplitudes a_b). Black dots indicate mean values, black lines are interpolated linearly for better visualization, and gray areas indicate standard deviations per the experimental repetitions. Parameter K_t is the transmission coefficient and λ is the spacing between roughness elements.

Figure 5. Spatial (i.e., vertical) and temporal distributions of the phase-averaged horizontal velocity $\tilde{u}$ [m/s] and the turbulent kinetic energy TKE [m²/s²] over the height z [m] in the near-bed region and a dimensionless wave cycle t/T_m [-]. Records at the beginning of the tested surfaces (x_{0L} = 35.5 m; see Figure B1 for positions x_{1L}, x_{2L}, and x_{5L}) are shown, sorted by bed surface configurations ($SC1$: *semicircle 1, M1*: *mix 1, L1*: *lamella 1, SC2*: *semicircle 2, M2*: *mix 2, L2*: *lamella 2*) and hydrodynamic cases (mean wave period T_m and near-bed horizontal wave excursion amplitudes a_b). Parameter z is the height above the peak of the roughness elements or the bed surface (case REF), t is the time step, and λ is the spacing between roughness elements. Color scales: $\tilde{u}$: red to blue; TKE: yellow to green (Crameri, 2018); white areas: data was deleted by filtering or not recorded.

trough (t/T = 0–0.5), then under the wave crest (t/T_m = 0.5–1.0) are shown. Generally, the largest negative velocities develop under the wave trough, and the largest positive velocities under the wave crest.

Above all tested ultra-rough bed surface surrogates, the vertical distributions of $\tilde{u}$ reveal increased residual velocity close to the roughness elements, corresponding to observations by, for example, Nielsen (1992) and Sumer and Fuhrman (2020). Furthermore, a phase lag toward the roughness elements is apparent in the vertical distributions of $\tilde{u}$. These trends are most pronounced for *L2* and *M2*, with sharp edges and large spacing λ_2, followed by *L1* and *M1*, with sharp edges and small spacing λ_1. For *SC1* and *SC2*, with bluntly-shaped roughness elements, these trends, especially the phase lag, are less pronounced. The *REF* case exhibits marginal levels of increased residual velocities and no noticeable phase lag.

TKE is generated above all ultra-rough bed surface surrogates, with maximum values near the bed surfaces decreasing with the distance from the roughness elements z. The sharp-edged surfaces cause significantly stronger turbulence than the bluntly-shaped and the *REF* surfaces. Furthermore, the *lamella*-type surfaces induce more turbulence than the *mix*-type surfaces. *SC2* is notable, as *TKE* production increases significantly for the case with a_b = 0.12 m compared to the cases with lower a_b. The furthest vertical extents of *TKE* can be observed for *L2*, followed by *M2*, *L1*, *M1*, and *SC2*, where *TKE* only develops for cases with larger a_b. The vertical extents of *TKE* for *SC1* and *REF* are significantly lower. Considering the temporal distributions of the *TKE*, differences can be observed depending on the ratio λ/a_b. For the larger values of λ/a_b = 1.4–5.0, intrawave variations can be observed. Bursts of high *TKE* occur at the same t/T_m as the maximum positive $\tilde{u}$ and partially at t/T_m of the maximum negative residual velocity, separated by intervals of low *TKE*, indicating that the turbulence fully dissipates within one wave cycle. With increasing λ/a_b, the bursts become more isolated. However, this trend is superimposed with the increasing *TKE* production caused by the rougher surface elements, that is, from the *semicircle*-over the *mix*-to the *lamella*-type surfaces. Hence, for the cases of *L2*, the bursts are less prominent compared to *M2* and *SC2*, as the overall *TKE* production is more substantial. For the ratios λ/a_b = 0.8–1.1, *TKE* is uniformly distributed over the entire wave cycle. Hence, the turbulence does not fully dissipate.

The differences in the vertical distributions of $\tilde{u}$ and *TKE* between the bed surface configurations further support the hypothesis that the sharp edges of the roughness elements are a governing cause for turbulence production, hence, frictional energy dissipation. Furthermore, the development of bursts of high *TKE* for λ/a_b > 1.1 in the temporal distribution clearly indicates that the spacings between the roughness elements also strongly influence wave energy dissipation.

After analyzing the temporal distributions, the maximum positive and negative amplitudes of the horizontal orbital velocity, $\tilde{u}_{max}/u_b$ and $\tilde{u}_{min}/u_b$ normalized by the maximum near-bed wave orbital horizontal velocity amplitude u_b have been determined across the water column (black, dotted lines). Hereby, $\tilde{u}_{max}$ and $\tilde{u}_{min}$ are defined as the mean of the 5% highest and lowest values of $\tilde{u}$ (Figure 5), respectively, to eliminate outliers, thus not necessarily occurring at the same t/T_m. A comparison to the normalized theoretical maximum positive and negative horizontal velocity amplitudes, according to Stokes second-order wave theory (Le Méhauté, 1976), $u_{Stokes,max}/u_b$ and $u_{Stokes,min}/u_b$ (gray, solid lines in Figure 6), reveals disagreement between the observed and theoretical velocity profiles. Furthermore, the vertical distribution of the normalized time-averaged horizontal velocity $\overline{u}/u_b$ (red, dotted line) is considered.

Regarding $\tilde{u}_{max}$ and $\tilde{u}_{min}$, all tested cases show velocity overshoots in the near-bed region. With increasing distance from the bed surface, the measured $\tilde{u}_{max}/u_b$ and $\tilde{u}_{min}/u_b$ approach the theoretical $u_{Stokes,max}/u_b$ and $u_{Stokes,min}/u_b$, respectively, while close to the bed surface, $\tilde{u}_{max}/u_b$ and $\tilde{u}_{min}/u_b$ exceed the theoretical values. The deviations between measured and theoretical values are more pronounced for the tested bed surfaces with large λ_2 (*L2*, *M2*, and *SC2*) than those with small λ_1 (*L1*, *M1*, and *SC1*).

The thickness of the boundary layer δ (horizontal, dashed gray lines in Figure 6; values listed in Table C2) is determined by comparing the measured and theoretical maximum horizontal velocity amplitudes. Following Sleath (1987) and Nielsen (1992), δ is defined as the height at which the difference between measured $\tilde{u}_{max}$ is less than one percent of the theoretical $u_{Stokes,max}$. Due to the vertical distortions and some scatter in the measured profiles, δ was determined visually as the first location above the bed surface, where $\tilde{u}_{max} \approx u_{Stokes,max}$. The thickest boundary layers form over *L2* (δ = 0.065–0.074 m), followed by *M2* (δ = 0.050–0.070 m), *L1* (δ = 0.040–0.051 m), *M1* (δ = 0.045–0.050 m), *SC2* (δ = 0.036–0.060 m), and *SC1* (δ = 0.019–0.027 m). For *REF*, the boundary layer is significantly thinner
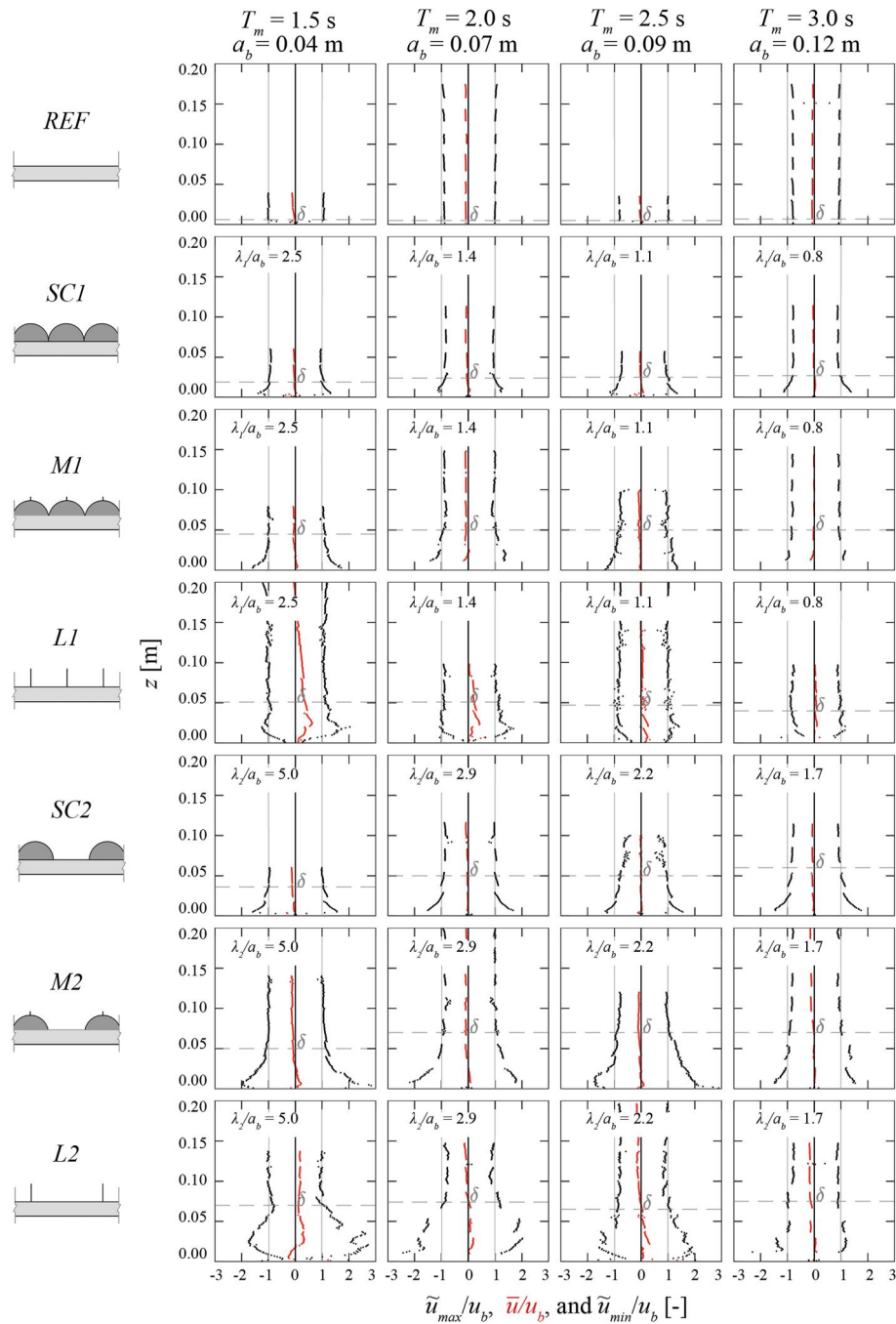
Figure 6. Vertical distribution of the maximum positive and negative phase-averaged horizontal orbital velocity amplitudes normalized by the maximum near-bed wave orbital horizontal velocity amplitude, $\tilde{u}_{max}/u_b$ and $\tilde{u}_{min}/u_b$ (black, dotted lines) [-],the normalized theoretical maximum positive and negative horizontal velocity amplitudes according to Stokes second-order wave theory, $u_{Stokes,max}/u_b$ and $u_{Stokes,min}/u_b$, [-] (gray, solid line), and the normalized time-averaged horizontal velocity $\overline{u}/u_b$ [-] (red, dotted line) over the height z [m] in the near-bed region. Records from the beginning of the tested surfaces (x_{0L} = 35.5 m; see Figure B2 for positions x_{1L}, x_{2L}, and x_{5L}) are shown, sorted bed surface configurations (SC1: semicircle 1, M1: mix 1, L1: lamella 1, SC2: semicircle 2, M2: mix 2, L2: lamella 2) and hydrodynamic cases (mean wave period T_m and near-bed horizontal wave excursion amplitudes a_b). The parameter λ is the spacing between roughness elements. The horizontal, dashed gray lines mark the thickness of the boundary layer δ, visually determined.

with δ = 0.005–0.007 m. The different hydrodynamic cases do not considerably impact δ for all tested surfaces.

The vertical profiles of $\tilde{u}_{max}/u_b$ and $\tilde{u}_{min}/u_b$ of the *semicircle*-type surfaces exhibit constantly increasing ratios until directly adjacent to the edges of the roughness elements, reaching maximum overshoots between 1.4 and

1.6 with similar shapes for all a_b. For the *lamella*-type surfaces, the maximum values of the overshoots are reached at a distance of $z \sim \delta/2$ to the edges of the roughness elements with gradually decreasing values of $\tilde{u}_{max}/u_b$ and $\tilde{u}_{min}/u_b$ below. Furthermore, the maximum overshoots decrease with increasing a_b from 2.1, 2.0, 1.6 to 1.2 and 2.8, 2.4, 2.1, 2.1, for *L1* and *L2*, respectively. The *mix*-type surfaces exhibit the highest overshoots, partly directly at the edges of the roughness elements and at $z \leq \delta/2$. Similar to the *lamella*-type surfaces, the maximum overshoots decrease with increasing a_b from 2.4, 1.9, 1.8 to 1.4 and 2.6, 2.1, 2.6, 2.0, for *M1* and *M2*, respectively (where the cases of *M2* with $a_b = 0.04$ and 0.09 m some scattered data is neglected). Above *REF*, overshoots between 1.0 and 1.1 develop. The velocity overshoots induced by all bed surface configurations are significantly larger than typical overshoots (up to 1.1; Sumer and Fuhrman (2020)) and are a strong indication of the development of periodic vortices around the edges of the roughness elements.

The vertical distributions of $\overline{u}/u_b$ exhibit slightly negative values at greater distances from the bed surface with average values of -0.03. Near the roughness elements, $\overline{u}/u_b$ increases, reaching zero for *REF* and positive values for all tested surfaces. The highest values are found for the lamella-type surfaces (*L2*: $(\overline{u}/u_b)_{max} = 0.30$–$0.80$ and *L1*: $(\overline{u}/u_b)_{max} = 0.11$–$0.47$), moderate values are found for the mix-type surfaces (*M2*: $(\overline{u}/u_b)_{max} = 0.12$–$0.43$ and *M1*: $(\overline{u}/u_b)_{max} = 0.04$–$0.36$). In contrast, the semicircle-type surfaces exhibit significantly lower values (*SC2*: $(\overline{u}/u_b)_{max} = 0.02$–$0.06$ and *SC1*: $(\overline{u}/u_b)_{max} = 0.00$–$0.03$). Notably, in all cases, $(\overline{u}/u_b)_{max}$ increases as a_b decreases.

The nonzero distributions of $\overline{u}/u_b$ can be explained by two competing effects. Non-linear waves exhibit skewed, that is, asymmetric, surface-level elevations and free-stream velocity profiles, causing turbulence asymmetry between the two half-cycles, which leads to steady streaming in the opposite direction of the wave propagation (Ribberink & Al-Salem, 1995; Scandura, 2007). Secondly, the bed friction causes a phase difference between the horizontal and vertical flow components, leading to a net, nonzero streaming in the direction of the wave propagation, referred to as the Longuet-Higgins streaming (Longuet-Higgins, 1953).

Figure 7 visualizes the vertical distribution of the maximum turbulent kinetic energy, TKE_{max}, normalized by the square of the maximum near-bed wave orbital horizontal velocity amplitude u_b^2. TKE_{max} was determined analogously to $\tilde{u}_{max}$, defined as the mean of the 5% highest values of TKE (Figure 5). TKE_{max}/u_b^2 is highest within the boundary layer for all surfaces, decreasing with increasing distance z until approaching zero. Hereby, the vertical profiles of TKE_{max}/u_b^2 exhibit variations appearing as parabolic shapes across each individual measurement, causing neighboring measurements to not align perfectly. Such parabolic shapes in the measurement of higher flow statistics with the VP have been documented in several studies (Lacey et al., 2018; MacVicar et al., 2014; Thomas et al., 2017). In the context of this study, these deviations have been deemed acceptable. Moreover, as the magnitude of TKE_{max} increases, the scatter in the distribution also increases, which can also be attributed to the limitations of the VP regarding turbulence measurements. Consequently, outliers in the vertical distribution of TKE_{max} have been eliminated by applying a gradient filter with a cutoff numerical gradient of two.

The magnitude of the TKE_{max}/u_b^2 distribution is highest near the edges of the roughness elements for all tested cases. The maximum near-bed turbulent kinetic energy $TKE_{max,b}$ is defined as the mean of the three highest values in the vertical distribution of TKE_{max}, which are within δ for all cases and configurations (values listed in Table C2). $TKE_{max,b}/u_b^2$ is largest for the sharp-edged surfaces, with the highest values for *L2* ($TKE_{max,b}/u_b^2 = 1.50$; 0.72; 0.72; 0.41), followed by *L1* ($TKE_{max,b}/u_b^2 = 1.4$; 0.59; 0.56; 0.26), *M2* ($TKE_{max,b}/u_b^2 = 0.73$; 0.54; 0.45; 0.37), followed by *M1* ($TKE_{max,b}/u_b^2 = 0.62$; 0.33; 0.34; 0.19) with decreasing values with increasing a_b. *SC2* ($TKE_{max,b}/u_b^2 = 0.07$; 0.08; 0.09; 0.18), and *SC1* ($TKE_{max,b}/u_b^2 = 0.03$; 0.08; 0.10; 0.06), yield significantly lower values of $TKE_{max,b}/u_b^2$. While $TKE_{max,b}/u_b^2$ for *SC1* remain largely constant, the values of *SC2* increase with increasing a_b, contrary to the trend observed for the cases with sharp-edged surfaces. Simultaneously, $TKE_{max,b}/u_b^2$ of *SC2* with $a_b = 0.12$ m is significantly higher than for the remaining cases with lower a_b. As expected, *REF* causes no visual TKE production in the water column. The vertical extent of TKE_{max} in the water column is also highest for the sharp-edged surfaces. Extents of TKE_{max}/u_b^2 for *L2* and *M2*, followed by *L1* and *M1*, exceed the thickness of the boundary layer δ. For *SC2* and *SC1*, the vertical extents of TKE_{max}/u_b^2 are significantly lower and lie within δ. The case *SC2* with $a_b = 0.12$ m is an exception, as TKE_{max}/u_b^2 is notable above the boundary layer, reaching similar extents as *L1* and *M1*.

Overall, it has been found that above all tested ultra-rough bed surface surrogates, a boundary layer forms based on the definition by Sleath (1987). The periodical wave-related component of the horizontal velocity $\tilde{u}/u_b$ and the vertical extents of δ do not differ significantly between the different roughness elements. In contrast, the
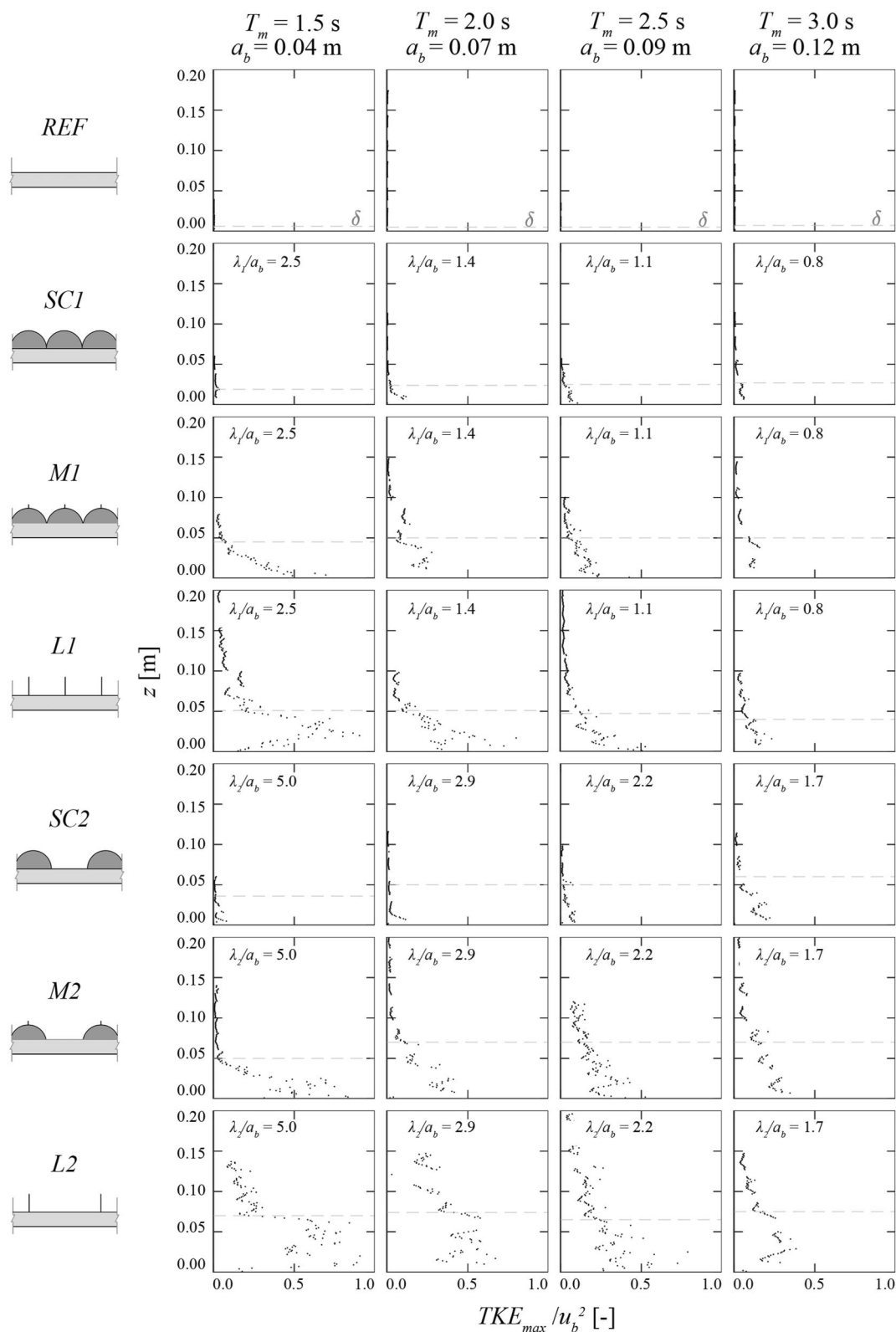
Figure 7.

turbulence production, visualized by $TKE_{max}/u_b{}^2$, is strongly influenced by the shape of the roughness elements and their spacing. The *lamella*-type surfaces induce $TKE_{max,b}/u_b{}^2$ 2 to 27 times larger turbulence production than the *semicircle* configurations, while the *mix* configurations still induce $TKE_{max,b}/u_b{}^2$ 1 to 18 times larger.

### 3.3. Quantification of Frictional Wave Energy Dissipation

Estimates of the wave friction factor f_w, the hydraulic roughness length k_w, and the maximum bed shear stress $\tau_{w,max}$ by both the EB and TKE methods are presented in Figure 8. For the EB method, the water surface elevations are analyzed by applying Equations 4–12. For the TKE method, the near-bed velocities are analyzed. The maximum bed shear stress $\tau_{w,max}$ has been calculated from $TKE_{max,b}$ by applying Equation 18. The parameters f_w and k_w have been determined by rearranging Equations 12 and 9.

For both methods, the *lamella*-type surfaces yield the most considerable hydraulic roughness, closely followed by the *mix*-type surfaces, while *semicircle*-type surfaces result in significantly smaller values. The largest values of f_w, k_s, and $\tau_{w,max}$ are found for *L2*, closely followed by *L1*, *M2*, and *M1*; the sharp-edged surfaces. The bluntly-shaped surfaces, *SC2* and *SC1* yield significantly smaller values for all three parameters. However, the absolute values of the three parameters resulting from the EB method reach, on average, 1.4 to 2.2 times the magnitude of those resulting from the TKE method (1.4 times for f_w, 1.7 times for k_w, and 2.2 times for $\tau_{w,max}$).

For the sharp-edged surfaces, the wave friction factor f_w increases with increasing ratio λ/a_b, where the cases with the largest λ/a_b exhibit f_w values 2 to 5 times larger than for the smaller λ/a_b. For the bluntly-shaped surfaces, f_w is constantly low. The hydraulic roughness length k_w reaches the highest values in cases with moderate λ/a_b ratios ($\lambda_1/a_b = 1.1$–1.4 for *L1*, *M1*, and *SC1* and $\lambda_2/a_b = 2.9$–2.2 for *L2*, *M2*, and *SC2*) for most configurations. *SC2* is an exception, where the case of the smallest $\lambda_2/a_b = 1.7$ is significantly larger than the remaining k_w values. Comparing k_w with the total roughness length $k_t = 0.050$ m (dashed gray lines in Figures 8c and 8d) for the sharp-edged surfaces reveals differences between the two estimation methods. According to the EB method, k_w induced by the sharp-edged surfaces reaches up to twice the height for the *lamella*-type surfaces and similar extents for the *mix*-type surfaces. In contrast, according to the TKE method, most k_w values are smaller than k_t, with the exception of the cases of *L1* and *L2* with the smallest λ/a_b, which reach similar extents as k_t. The bluntly-shaped surfaces induce significantly lower k_w with only 1%–13% of k_t, except for the case of *SC2* with $\lambda_2/a_b = 1.7$, which reaches up to 32% and 38% of k_t for the EB and the TKE method, respectively. Considering the maximum bed shear stress, following the EB method, for the cases of *L2*, *L1*, and *M1*, the largest $\tau_{w,max}$ values result from cases with $\lambda_1/a_b = 1.4$ or $\lambda_2/a_b = 2.9$, similar to the trend of k_w, while for *M2*, *SC1*, and *SC2*, the smallest $\lambda_1/a_b = 0.8$ and $\lambda_2/a_b = 1.7$ induced largest $\tau_{w,max}$ values. Furthermore, the case of *SC2* with $\lambda_2/a_b = 1.7$ is striking, as the $\tau_{w,max}$ is significantly larger than for the remaining cases. As for the TKE method, the values of $\tau_{w,max}$ are generally constant for cases with $\lambda_1/a_b = 1.4$–0.8 and $\lambda_2/a_b = 1.7$–2.9 with slightly smaller values for $\lambda_1/a_b = 2.5$ and $\lambda_2/a_b = 5.0$, respectively. In the cases of *SC2*, $\tau_{w,max}$ values increase significantly for the lowest $\lambda_2/a_b = 1.7$, similar to the observations of the EB method. The substantial increase in $\tau_{w,max}$ reflects the development of turbulent bursts for $\lambda/a_b = 1.7$ (see Figure 5).

The EB method reveals that the experiments with the *lamella*-type surfaces reach values of f_w, k_w, and, $\tau_{w,max}$ that are 6–45, 10–140, and 5–37 times larger than those with the *semicircle*-type surfaces, respectively, without considering *SC2* with $a_b = 0.12$ m as an exception. Similarly, the experiments with the *mix*-type surfaces yield values of f_w, k_w, and, $\tau_{w,max}$ that are 5–35, 8–100, and 4–9 times larger than those with the *semicircle*-type surfaces, respectively. For the TKE method, the *lamella*-type surfaces reach values of f_w, k_w, and $\tau_{w,max}$ that are 2–39, 10 to 250, and 2 to 27 times larger than those of the *semicircle* configurations, respectively. Likewise, the *mix*-type surfaces yield values of f_w, k_w, and $\tau_{w,max}$, which are 2–23, 10–150, and 1–18 times larger than those of the *semicircle*-type surfaces, respectively. These observations indicate that the sharp edges of the roughness elements are the primary cause of wave attenuation. The fact that the *mix* configurations result in only slightly smaller

Figure 7. Vertical distribution of the maximum turbulent kinetic energy normalized by the square of the maximum near-bed wave orbital horizontal velocity amplitude $TKE_{max}/u_b{}^2$ [-] for the near the bed region over the height z [m]. Records from the beginning of the tested surfaces ($x_{0L} = 35.5$ m; see Figure B3 for positions x_{1L}, x_{2L}, and x_{5L}) are shown, sorted by bed surface configurations (*SC1*: *semicircle 1*, *M1*: *mix 1*, *L1*: *lamella 1*, *SC2*: *semicircle 2*, *M2*: *mix 2*, *L2*: *lamella 2*) and hydrodynamic cases (mean wave period T_m and near-bed horizontal wave excursion amplitudes a_b). The parameter λ is the spacing between roughness elements. The horizontal, dashed gray lines mark the thickness of the boundary layer δ, visually determined.
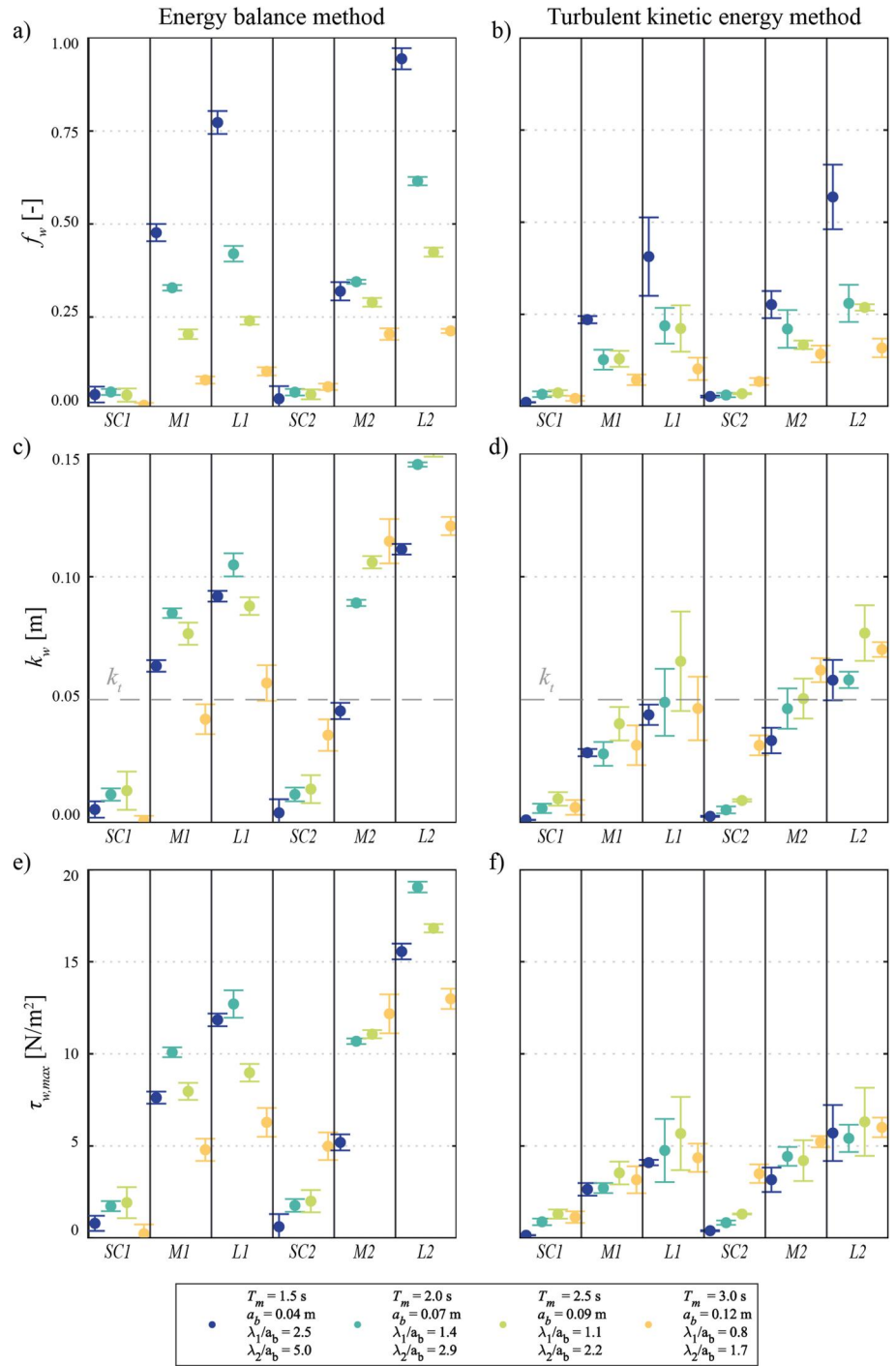
Figure 8. Averaged values and standard deviations of (a) and (b) the wave friction factors f_w, (c) and (d) the hydraulic roughness length k_w, and (e) and (f) the bed shear stresses $\tau_{w,max}$ determined by applying the energy balance (EB) and the turbulent kinetic energy (TKE) method. The results are sorted by bed surface configurations (*SC1*: *semicircle 1*, *M1*: *mix 1*, *L1*: *lamella 1*, *SC2*: *semicircle 2*, *M2*: *mix 2*, *L2*: *lamella 2*) and hydrodynamic cases (mean wave period T_m and near-bed horizontal wave excursion amplitudes a_b). The parameter λ is the spacing between roughness elements. The dashed gray line in (b) marks the total roughness height k_t of the roughness elements.

values than the *lamella* configurations suggests that the shape below the edge is less relevant. Comparing the same roughness elements with different spacings and varying a_b reveals that the highest hydraulic roughness is reached at $\lambda/a_b = 1.4$–2.9 for all tested ultra-rough bed surfaces. Smaller and larger λ/a_b induce smaller $\tau_{w,max}$ and k_w. The smallest $\tau_{w,max}$ values are found for $\lambda/a_b = 0.8$.

Figures 9a and 9b depict the flow regimes by correlating the relative roughness a_b/k_w with the wave-boundary layer Reynolds number Re, following Kamphuis (1975) for both the EB and TKE methods. Remarkably, the flow regimes exhibit substantial differences due to sharp-edged roughness elements compared to bluntly-shaped roughness elements, despite similar Re being maintained for each hydrodynamic case. The a_b/k_w ratios are significantly higher for the bluntly-shaped surfaces a_b/k_w (EB method: $a_b/k_w = 5.5$–129.2 and TKE method: $a_b/k_w = 5.0$–40.4) than those of the sharp-edged surfaces (EB method: $a_b/k_w = 0.4$–4.0 and TKE method: $a_b/k_w = 0.6$–4.7). Notably, the a_b/k_w ratios of the sharp-edged surfaces are in close agreement with those attributed to very large roughnesses ($0.2 < a_b/k_w < 4.0$) as defined by Dixen et al. (2008) and Sumer and Fuhrman (2020). All sharp-edged surfaces induce rough turbulent boundary layers for all hydrodynamic cases and for both methods, while for the bluntly-shaped surfaces, laminar to rough turbulent flow regimes are indicated depending on hydrodynamic conditions. The most notable discrepancy from the sharp-edged surfaces occurs for the case $a_b = 0.04$ m, where *SC1* exhibits a laminar boundary layer, and *SC2* shows either a laminar boundary layer or transition to turbulent boundary layer (EB and TKE method, respectively). The cases of *SC1* with $a_b = 0.07$–0.12 m and *SC2* with $a_b = 0.07$–0.09 m are situated at the borderline of the rough turbulent regime (EB method) or classified as transitional to the rough turbulent regime (TKE method). *SC2* with $a_b = 0.12$ m results in rough turbulent conditions for both methods. According to the EB method, the case of *SC1* with $a_b = 0.12$ m is situated in the transitional regime, indicating that f_w is influenced by both a_b/k_s and *Re*. Consequently, Equation 8 is not applicable to accurately determining the phase angle ϕ between f_e and f_w, leading to an overestimation of f_w. Given that the case borders the rough turbulent regime, the influence of *Re* is considered negligible. Nonetheless, it should be noted that f_w is slightly overestimated.

The assignment of a laminar boundary layer for *SC1* with $a_b = 0.04$ m is supported by the observation that *TKE* develops above all surfaces except *SC1* with $a_b = 0.04$ m (see Figure 7), indicating laminar conditions. Consequently, the frictional energy dissipation is low and reliant on the Reynolds number, while the relative roughness is of subordinate relevance (see Equations 8–12). The cases of *SC1* with $a_b = 0.07$–0.12 m and *SC2* with $a_b = 0.07$–0.09 m are assigned transitional to rough turbulent or rough turbulent boundary layers, reassured by the development of small levels of *TKE* for these cases (see Figure 7). The different flow regimes for these cases occur because distinct methods are chosen, which yield smaller k_w values for the TKE than the EB method and are not due to physical differences. Nevertheless, the discrepancies between methods suggest that the frictional wave dissipation may be influenced by both the Reynolds number and the relative roughness (see Equations 8–11). Turbulence production is markedly enhanced for the case of *SC2* with $a_b = 0.12$ m, resulting in significantly higher bed shear stresses compared to the other experiments with bluntly-shaped surfaces, justifying the explicit allocation to the rough turbulent flow regime. Hence, similar to the experiments with sharp-edged surfaces, the boundary layer is primarily dependent on the relative roughness, and the Reynolds number is of subordinate influence (see Equations 8–11). The magnitudes of $\tau_{w,max}$ substantiated the trends (see Figure 8), as $\tau_{w,max}$ is significantly higher for the cases assigned the rough turbulent regime than for those assigned the laminar or the transition to rough turbulent regimes. The significantly higher relative roughnesses of the cases with sharp-edged surfaces further confirm the influence of the sharp edges on the frictional energy dissipation.

4. Discussion

4.1. The Relative Spacing of Roughness Elements

The results obtained from this work highlight the complex interactions of the shape of the roughness elements, the spacing λ between elements, and the hydrodynamic conditions expressed by the near-bed horizontal wave excursion amplitude a_b and the maximum near-bed orbital velocity amplitude u_b, on the wave attenuation of ultra-rough bed surfaces in oscillating flows. Comparing the same roughness elements with varying λ reveals that larger λ induce higher wave attenuation for the sharp-edged surfaces, as evidenced in all investigated parameters. When examining the various hydrodynamic cases for the same λ, it is apparent that wave attenuation reaches the highest values at moderate $a_b = 0.07$–0.09 m for all sharp-edged surfaces, diminishing for both higher and lower a_b values. This observation is reassured as estimates of $\tau_{w,max}$ resulting from both the EB and the TKE method fall in
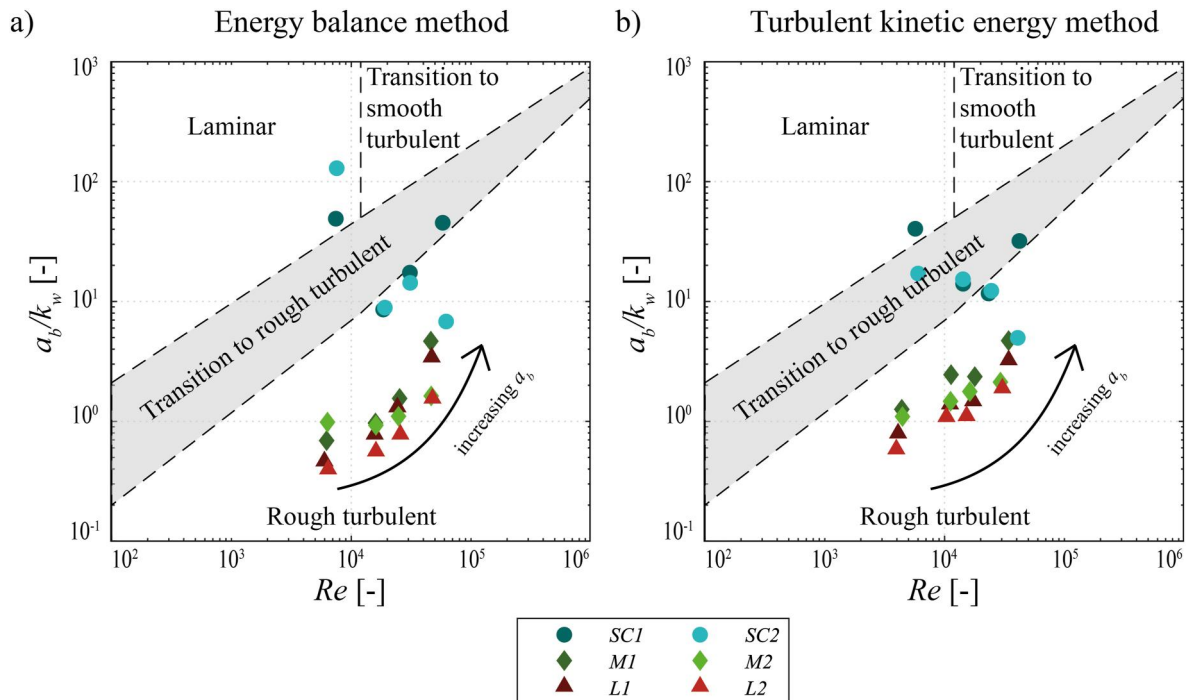
Figure 9. Flow regimes as defined by Kamphuis (1975) for (a) the energy balance method and (b) the turbulent kinetic energy method. The results are sorted by bed surface configurations (*SC1*: *semicircle 1*, *M1*: *mix 1*, *L1*: *lamella 1*, *SC2*: *semicircle 2*, *M2*: *mix 2*, *L2*: *lamella 2*). Dashed lines mark the limits between flow regimes, *Re* is the Reynolds number and a_b/k_w is the relative roughness.

the same range. Furthermore, the analysis of the near-bed velocities has shown that the maximum near-bed horizontal orbital velocity $\tilde{u}_{max}$ does not increase linearly with u_b, and the maximum near-bed turbulent kinetic energy $TKE_{max,b}$ does not increase linearly with u_b^2. Both ratios decrease with increasing u_b and u_b^2, respectively.

The observed trend that larger λ induce higher wave attenuation draws parallels to the extensively studied impact of varying roughness density subjected to unidirectional flows (Chung et al., 2021; Jiménez, 2004). A commonly applied concept is the differentiation of surface roughness subjected to steady, unidirectional flows in *k*- and *d*-type roughness, depending on the ratio of λ/k_t (or the frontal solidity; e.g., Schlichting (1936), Perry et al. (1969); Jiménez (2004); Chung et al. (2021)). In *k*-type roughness, roughness elements are sparsely arranged. Directly behind the elements, stable vortices form, and, at a certain distance, the streamlines reattach to the bed surface. The hydraulic roughness depends directly on the total roughness height k_t. In *d*-type roughness, the spacings between elements are narrow, leaving insufficient space for the streamlines to reattach to the bed surface behind the vortex formation. The hydraulic roughness becomes independent of k_t, and the frictional resistance decreases (Agelinchaab & Tachie, 2006; Chung et al., 2021). Hence, *k*-type roughness induces stronger flow resistance and energy dissipation than *d*-type roughness. In waves, the development of stable flow profiles is constantly interrupted by the oscillating nature of the flows (Nielsen, 1992; Sumer & Fuhrman, 2020). Since no stable vortices form behind the roughness elements as in unidirectional flows, a direct application of the concept is unfeasible.

Nevertheless, based on the observations found in this study, it is suggested that in oscillating flows, λ can be analogously considered to differentiate flow conditions similar to *d*- and *k*-type roughness. The relatively large *KC* numbers in the same order of magnitude as, for example, reported by Dixen et al. (2008) and velocity overshoots of $\tilde{u}_{max}/u_b$ suggest the formation of vortices (compare Table 1 and Figure 6). For the large spacings λ, bursts of turbulence can dissipate within the space (a_b) and time (T) provided by the waves. Hence, streamlines reattach to the bed surface after the vortices dissipate, and the hydraulic roughness depends directly on the total roughness height k_t. For small spacings λ_l, the a_b and T_m are too short for the turbulence to dissipate completely, indicated by the "residual" *TKE* in the temporal distributions of the phase-averaged *TKE* of the cases with $\lambda_l/a_b <$ 1.0. Hence, the streamlines do not reattach to the bed surface and become independent of k_t, which leads to smaller

k_w and, subsequently, smaller wave energy dissipation. These effects are visible in the vertical and temporal distributions of *TKE* in Figure 5; however, they are overshadowed by the overall increasing *TKE* production due to the sharp-edged surfaces.

Nonetheless, the observation that the highest rates of wave attenuation are reached at moderate $a_b = 0.07$–0.09 m remains unexplained. This observation aligns with the impact of varying densities of roughness elements (or the solid volume fractions) in submerged canopies under the same hydrodynamic conditions (Chung et al., 2021; Nepf, 1999, 2012). As the densities of roughness elements increase, the flow velocity $\overline{u}$ within the canopies experiences a decline, while changes in the *TKE* exhibit non-linear behavior due to the combined effects of increasing roughness density leading to enhanced turbulence production and decreasing $\overline{u}$ resulting in reduced turbulence production. Consequently, *TKE* initially increases with the rising density of roughness elements from zero but eventually reaches a threshold where a further increase in densities of roughness elements leads to a decline in *TKE*.

It is suggested that sharp-edged roughness elements in oscillating flows cause similar behavior. Hereby, the spacings between roughness elements resemble the density of roughness elements (expressed throughout this work by the relative spacings λ/a_b). Larger spacings result in less disturbance of the flow, leading to higher near-bed velocities and higher turbulence production. As a_b (and u_b) increases, the relative roughness density also increases, reaching a threshold of turbulence production between $a_b = 0.07$–0.09 m and maximum near-bed velocities. With higher a_b, the *TKE* production experiences a decline, reflecting the non-linear behavior of *TKE* in submerged canopies with increasing density of roughness elements. The differences in the intrawave turbulence dissipation reassure these observations, as for large relative spacings, *TKE* is completely dissipated, and for smaller relative spacings, residual *TKE* remains after one wave cycle, which adds to the total *TKE*, thus contributing to the non-linear behavior (see Section 3.2). As $\tau_{w,max}$ is directly proportional to $TKE_{max,b}$ (see Equation 18), the maximum bed shear stress exhibits the same non-linear behavior.

While these findings provide valuable insights into the complex interactions between the shape of roughness elements, their spacings, and the hydrodynamic conditions, the analysis of the water surface elevations and velocity profiles presented in this work, the frictional energy dissipation can only be determined implicitly. To further investigate the influence of the λ/a_b ratio on the discussed aspects, explicit determination of the bed shear stresses for a broader scope of hydrodynamic conditions and spacings between roughness elements should be topics of future investigations. Numerical simulations would allow explicit determination via the integration of pressure on the surrogate. Alternatively, volumetric time-resolved measurements of the flow field would allow a detailed investigation of the turbulence structures.

4.2. Comparison of Methods

Comparing the quantification of the frictional wave energy dissipation determined by the TKE and EB methods (see Section 3.3) reveals similar trends for both methods but different magnitudes of the investigated quantities. The results of the EB method are, on average, 1.4–2.2 times larger than those of the TKE method for the sharp-edged surfaces. Figure 10a) illustrates the differences between both methods in the example of the maximum bed shear stress $\tau_{w,max}$. Both methods display similar proportions between the bed surface configurations as the highest $\tau_{w,max}$ can be observed in the same order (*L2*, *L1*, *M2*, *M1*, and with significantly lower values *SC2* and *SC1*). Furthermore, some scatter of $\tau_{w,max}$ values between both methods is observable, increasing in intensity from the bluntly-shaped surfaces to the sharp-edged surfaces.

The EB method has been successfully employed to derive wave friction factors and bed shear stress estimates in several rough oceanic surfaces, for example, coral reefs (Lentz et al., 2016; Lowe et al., 2005), mussel beds (Donker et al., 2013), and seagrass meadows (Paul & Amos, 2011). Furthermore, secondary effects due to sidewall friction and other imperfections of the flume, which have caused difficulties in previous studies (Brevik & Bjørn, 1980; Hunt, 1952; Mirfenderesk & Young, 2003), have been successfully removed (see Section 2.3.1). It is, therefore, assumed that the resulting $\tau_{w,max,EB}$ provide the most accurate results.

The TKE method, initially developed for tidal currents (Soulsby, 1981), employs an empirically determined correlation factor $C = 0.19$ and has been proven to yield accurate results for a wide range of flow conditions and bed surfaces in unidirectional flows. However, Pope (2012) and Biron et al. (2004) conclude that the parameter C may vary close to the bed and needs to be re-estimated, especially for larger hydraulic roughnesses. A re-
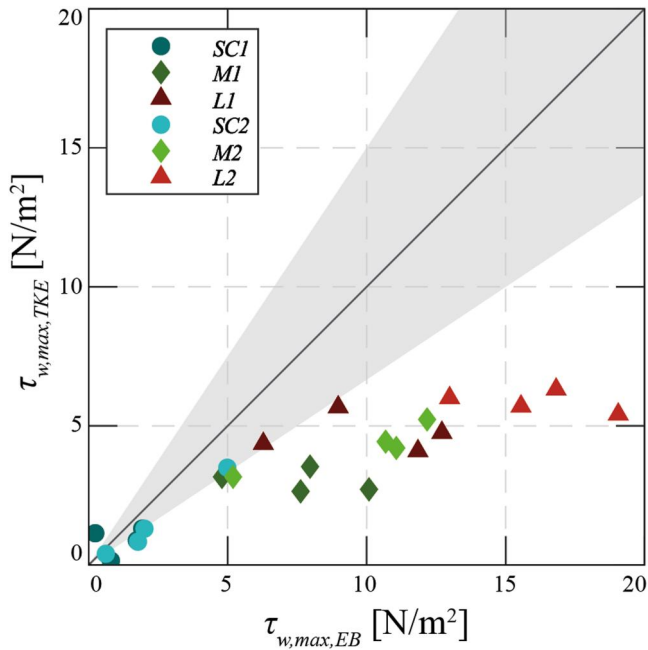
Figure 10. Comparison of the maximum bed shear stress $\tau_{w,max}$ determined by the energy balance method and the turbulent kinetic energy method. Gray areas mark deviations of ±50%. The tested ultra-rough bed surface configurations are indicated by dark blue circles: *semicircle 1* (*SC1*), light blue circles: *semicircle 2* (*SC2*), dark green diamonds: *mix 1* (*M1*), light green diamonds: *mix 2* (*M2*), *lamella 1* (*L1*), and light blue circles: *lamella 2* (*L2*).

estimation has been carried out by, for example, Zhang et al. (2020) for unidirectional flow in a 60° bend and the presence of a groyne resulting in an adjusted $C = 0.23$. In this study, an adjusted $C = 0.45$ would have been required to align the $\tau_{w,max,TKE}$ values to the $\tau_{w,max,EB}$ values. However, this value appears unreasonably high compared to typical ranges in the pertinent literature ($C = 0.19$–0.20), suggesting that not all relevant effects are accurately captured by the TKE method. Furthermore, to the authors' knowledge, the TKE method has only been applied by Thompson et al. (2012) to derive bed shear stress estimates in oscillatory flow for a single rough bed surface with significantly smaller roughness elements than those of this study (gravel bed with a mean particle size of $d_{50} = 11$ mm).

As outlined in Section 4.1, flow over large roughness elements exhibits highly spatially heterogeneous patterns. Several studies (Dixen et al., 2008; Ghodke & Apte, 2016; Giménez-Curto & Lera, 1996) concluded that in addition to the shear stress resulting from turbulent fluctuations in the flow, form-induced periodic stresses resulting from the separation and reattachment of the mean flow from the bed surface and the coherent formation of large-scale vortices become relevant for the wave energy dissipation. Hence, in addition to turbulent kinetic energy, momentum transfer occurs due to dispersive stresses resulting from the work of the mean flow against the pressure drag of each roughness element, expressed by the wake kinetic energy, *WKE* (Dunbar et al., 2023; Ghodke & Apte, 2016, 2018; Mignot et al., 2009; Raupach & Shaw, 1982). These dispersive stresses are not considered in the TKE method. The large velocity overshoots of $\tilde{u}_{max}/u_b$ and *KC* numbers (compare Table 1 and Figure 6) in the same order of magnitude as, for example, those reported by Dixen et al. (2008) suggest that dispersive stresses may become relevant in this study.

To capture the dispersive stresses, that is, the spatial variations in the near-bed flow properties, spatial averaging of the phase-averaged flow velocity components has been conducted, following Nikora et al. (2007) and Coleman et al. (2008). To establish the double-averaged velocity profiles, additional velocity profiles were recorded at three x-locations near $x_{L0} = 35.50$ m ($x_{L0,1} = 35.55$ m; $x_{L0,2} = 35.60$ m; and $x_{L0,3} = 35.65$ m) with a spacing of $\lambda_2/4 = 0.05$ m for the hydrodynamic cases with $T_m = 2.0$ and 3.0 s. For the bed surface configurations with λ_1, this results in an additional velocity profile above the crest of the subsequent roughness element ($x_{L0,2}$) and two velocity profiles in the centers of the roughness troughs ($x_{L0,1}$ and $x_{L0,3}$). For the bed surface configurations with λ_2, the three additional velocity profiles span the roughness trough (Figure D1). After applying the Reynolds decomposition to the instantaneous velocity components u_i, v_i, and w_i according to Eqs. (13)–(16) at each x-location, each component, for example, $u_i = \overline{u} + \tilde{u} + u'$ in the stream-wise direction, can be further decomposed into spatially-averaged and spatially-fluctuating components. These are denoted $\overline{u} = \langle \overline{u} \rangle + \hat{u}$, $\tilde{u} = \langle \tilde{u} \rangle + \widehat{\tilde{u}}$, and $u' = \langle u' \rangle + \widehat{u'}$, where the angle brackets denote the spatial averaging of the flow component, and the angle overbars denote the spatial fluctuations. The instantaneous velocity can be generally expressed as:

$$u_i = \langle \overline{u} \rangle + \hat{u} + \langle \tilde{u} \rangle + \widehat{\tilde{u}} + \langle u' \rangle + \widehat{u'}. \tag{19}$$

The lateral and bottom-normal velocity components have been decomposed similarly. Next, double-averaged turbulent kinetic energy, $\langle TKE \rangle$ (per mass unit) has been determined as follows:

$$\langle TKE \rangle = \frac{1}{2} \cdot \left(\overline{\langle u'^2 \rangle} + \overline{\langle v'^2 \rangle} + \overline{\langle w'^2 \rangle} \right). \tag{20}$$

Vertical distributions of the individual $\tilde{u}_{max}/u_b$, $\tilde{u}_{min}/u_b$, $\overline{u}/u_b$, and TKE_{max}/u_b^2 at the four x-locations, and the double averaged $\langle \tilde{u} \rangle_{max}/u_b$, $\langle \tilde{u} \rangle_{min}/u_b$, $\langle \overline{u} \rangle/u_b$, and $\langle TKE \rangle_{max}/u_b^2$ are shown in Figure D1. The wake kinetic energy $\langle WKE \rangle$ (per mass unit), as an additional significant contribution to the bed shear stress is determined analogously to $\langle TKE \rangle$:

$$\langle WKE \rangle = \frac{1}{2} \cdot \left(\langle \tilde{u}\tilde{u} \rangle + \langle \tilde{v}\tilde{v} \rangle + \langle \tilde{w}\tilde{w} \rangle \right). \tag{21}$$

The vertical distributions of the maximum double-averaged turbulent and the wake kinetic energies, $\langle TKE \rangle_{max}^{2}$ and $\langle WKE \rangle_{max}$ (Figure 11 and Table D1), respectively, have been determined similarly to TKE_{max} (compare Figure 7). Above the crest of the roughness elements, the distributions of $\langle TKE \rangle_{max}$ resemble those of TKE_{max}. Below the roughness crest, $\langle TKE \rangle_{max}$ decreases rapidly, approaching zero. The vertical distributions of $\langle WKE \rangle_{max}$ yield maximum values directly at the crest of the roughness elements and diminishes shortly above and below, with smaller vertical extents as $\langle TKE \rangle_{max}$, as observed by, for example, Dunbar et al. (2023). The normalized maximum near-bed values $\langle TKE \rangle_{b,max}/u_b^{2}$ are the highest for the sharp-edged surfaces (*L2, M2, L1,* and *M1*) and significantly lower values for the bluntly-shaped surfaces *SC2* and *SC1*. Hereby, $\langle TKE \rangle_{b,max}$ is on average 1.4 times larger than $TKE_{b,max}$. Likewise, maximum values of the maximum near-bed $\langle WKE \rangle_{b,max}$ are found for the sharp-edged surfaces in the same order (*L2, M2, L1, M1, SC2,* and *SC1*). For the bluntly-shaped surfaces, the wake kinetic energy is larger than the turbulent kinetic energy, as values of $\langle TKE \rangle_{b,max}$ reach 0.8 of the $\langle WKE \rangle_{b,max}$ values, while for the sharp-edged surfaces, the turbulent kinetic energy becomes dominant, as values of $\langle TKE \rangle_{b,max}$ reach 1.2 and 1.9 of the $\langle WKE \rangle_{b,max}$ values for mix and lamella configurations, respectively.

The maximum bed shear stress $\tau_{w,max,\langle TKE \rangle + \langle WKE \rangle}$, as the sum of the shear stresses arising from the maximum double-averaged near-bed turbulent kinetic energy, $\langle TKE \rangle_{b,max}$, and the maximum double-averaged near-bed wake kinetic energy, $\langle WKE \rangle_{b,max}$, is calculated as follows:

$$\tau_{w,max,\langle TKE \rangle + \langle WKE \rangle} = \langle \tau_{TKE,max} \rangle + \langle \tau_{WKE,max} \rangle = C \cdot \rho \cdot \left(\langle TKE \rangle_{b,max} + \langle WKE \rangle_{b,max} \right), \tag{22}$$

where the same correlation factor $C = 0.19$ is applied for $\langle \tau_{WKE,max} \rangle$ as for $\langle \tau_{TKE,max} \rangle$. From now on, the outlined method is referred to as TKE-WKE method.

In Figure 12a the maximum bed shear stress estimates of the TKE-WKE method are plotted against those of EB method. Despite a significant scatter of up to $\pm 50\%$, the comparison shows the same order of magnitude between the two methods. The deviations may be attributed to the inherent limitations of the turbulence measurement by the VP and the restricted number of analyzed velocity profiles across the bed surface, especially for the bed surface configurations with λ_I. Given the significant scatter, the results should be considered a preliminary assessment. Nonetheless, the promising agreement suggests that further investigation is warranted. For a more in-depth analysis and validation, numerical simulations or volumetric time-resolved measurements of the flow field, such as particle image velocimetry or particle tracking velocimetry, would offer more detailed insights and validation of the approach.

4.3. Application to Oyster Reefs

A direct comparison of this work's estimated roughness parameters to other studies regarding oyster reefs is not feasible as, to the authors' knowledge, wave energy dissipation due to bed friction in oscillating flow has not yet been investigated thoroughly. Borsje et al. (2011) report substantial wave energy attenuation of an oyster reef and a mussel bed surface. However, it is essential to consider that the hydrodynamic conditions were chosen to illustrate the distinct behavior of the two oceanic surfaces and not to depict relevant hydrodynamic conditions for wave attenuation with very shallow submergence ($d/k_t = 3.6$) and low wave height compared to the size of the oyster and mussel shells. A comparison of the transmission coefficients with those obtained in this study indicates wave attenuation up to 15 times higher. However, due to the different submergence and wave heights, the results are not directly comparable to those of this study. However, this study's estimated values of f_w fall within the range of other oceanic surfaces. The f_w values of the bluntly-shaped surfaces ($f_w = 0.00\text{–}0.06$) compare to the estimates of the mussel bed reported by Donker et al. (2013) and to those of a seagrass meadow ($f_w = 0.02\text{–}0.08$) reported by Paul and Amos (2011)). The f_w values of the sharp-edged surfaces ($f_w = 0.10\text{–}0.94$) compare to estimates for coral reefs ($f_w = 0.1\text{–}0.4$ (Harris et al., 2018; Lowe et al., 2005; Monismith et al., 2013; Nelson, 1996) or up to $f_w = 1.8$ (Monismith et al., 2015)) as a comparable ultra-rough oceanic surface. The estimates of f_w for a rippled bed by Mirfenderesk and Young (2003) ($f_w = 0.33$ for $d = 0.44$ m, $T_m = 2.0$ s, $H_m = 0.087$ m) are in close agreement with those of *M1* with comparable hydrodynamic conditions ($f_w = 0.329 \pm 0.007$ for $T_m = 2.0$ s and $a_b = 0.07$ m). Mathisen and Madsen (1996) report $f_w = 0.31 \pm 0.06$ and $f_w = 0.19 \pm 0.02$ for similar rippled beds
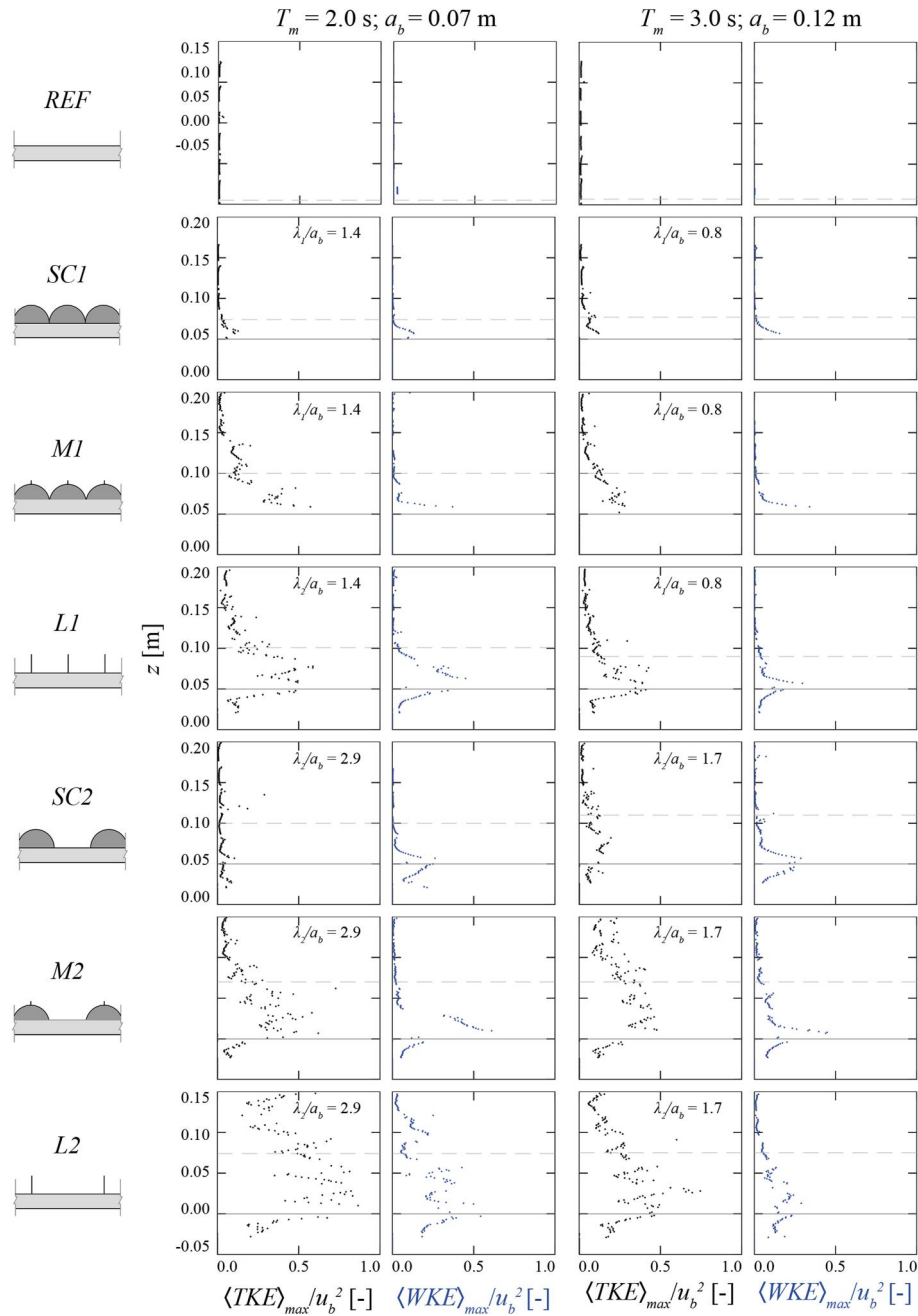
Figure 11. Vertical distribution of the maximum turbulent kinetic energy and the maximum wake kinetic energy normalized by the square of the maximum near-bed wave orbital horizontal velocity amplitude, $\langle TKE \rangle_{max}/u_b^2$ and $\langle WKE \rangle_{max}/u_b^2$ [-], for the near the bed region over the height z [m]. Records from the beginning of the tested surfaces ($x_{0L} = 35.5$ m) are shown, sorted bed surface configurations (SC1: *semicircle 1*, M1: *mix 1*, L1: *lamella 1*, SC2: *semicircle 2*, M2: *mix 2*, L2: *lamella 2*) and hydrodynamic cases (mean wave period T_m and near-bed horizontal wave excursion amplitudes a_b). The parameter λ is the spacing between roughness elements. The horizontal solid black lines mark the height of the roughness elements ($z = 0$), and the horizontal, dashed gray lines mark the thickness of the boundary layer δ, visually determined.

with 0.1 and 0.2 m spacing, respectively, for $T = 2.59 \pm 0.28$ s and $a_b = 0.051 \pm 0.006$ m. These estimates compare to those of *M1* ($f_w = 0.204 \pm 0.013$) and *M2* ($f_w = 0.290 \pm 0.012$) in similar hydrodynamic conditions ($T_m = 2.5$ s and $a_b = 0.09$ m). However, while Mathisen and Madsen (1996) report lower f_w values for larger spacing, the results of this study suggest higher f_w values for larger spacings. One plausible explanation for the observed differences could stem from the different shapes and significantly smaller roughness elements, as the sharp edges of the *mix*-type surfaces induce more turbulence with higher near-bed velocities and the consequent
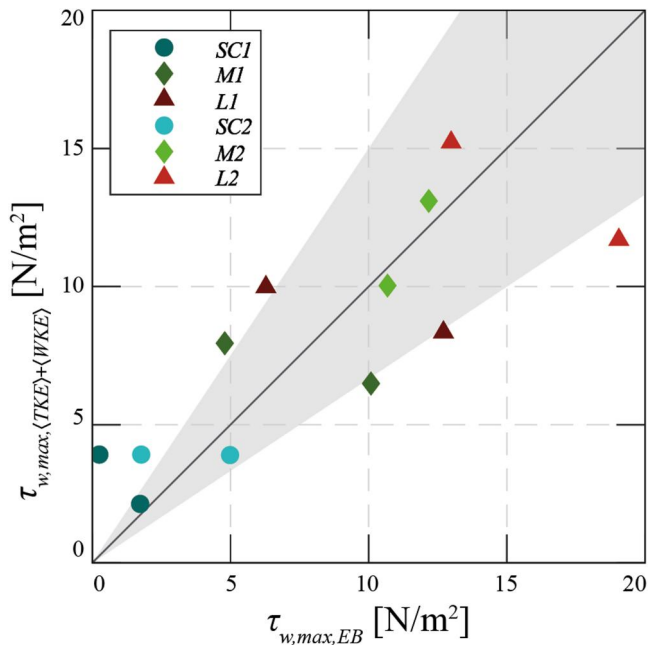
Figure 12. Comparison of the maximum bed shear stress $\tau_{w,max}$ determined by the energy balance method ($\tau_{w,max,EB}$) and the TKE-WKE method ($\tau_{w,max,\langle TKE \rangle + \langle WKE \rangle}$). Gray areas mark deviations of ±50%. The tested ultra-rough bed surface configurations are indicated by dark blue circles: *semicircle 1* (*SC1*), light blue circles: *semicircle 2* (*SC2*), dark green diamonds: *mix 1* (*M1*), light green diamonds: *mix 2* (*M2*), *lamella 1* (*L1*), and light blue circles: *lamella 2* (*L2*).

non-linear behavior of turbulence production as the tips of the triangular bars. Furthermore, the large velocity overshoots reported for the sharp-edged roughness elements may induce stronger dissipative stresses than the triangular-shaped roughness elements, adding to the total wave energy dissipation.

Morris et al. (2021) point out that most constructed oyster reefs, as part of nature-based coastal protection strategies, are narrow and low-crested structures that are ineffective at attenuating waves. In most constructed reefs, wave attenuation is mainly induced by wave breaking, so the main focus in the design process is put on the reef crest height relative to the water depth and wave height (Chowdhury et al., 2019; Wiberg et al., 2019; Zhu et al., 2020). However, the ultra-rough reef surfaces show considerable potential to attenuate waves effectively due to bed friction, especially when waves are allowed to propagate for at least a couple of wavelengths. The results of this study illustrate that surfaces with sharp-edged roughness elements, such as oyster reef surfaces, significantly increase the bed friction and the induced wave energy dissipation compared to smooth surfaces or even to surfaces with bluntly-shaped roughness elements of the same size. Bed shear stresses and wave friction factors induced by the tested sharp-edged surfaces in this study are up to 4–35 times higher than those of the bluntly-shaped surfaces.

Therefore, future designs of oyster reefs as NbS should consider optimized conditions for frictional dissipation due to bed friction, that is, enlarged oyster reef widths or patch layouts, to increase their effectiveness. Primarily, wider structures should be considered to extend the interaction length between waves and bed surface, as Morris et al. (2021) suggest. This observation is in line with studies on rubble-mound breakwaters (Seabrook & Hall, 1998) and bagged oyster shell reefs (Allen & Webb, 2011), illustrating that wider structures cause considerably higher wave attenuation. However, as the cost of construction increases with surface area, a balance must be struck between the cost and benefit of wider constructed reefs. In natural-occurring, spatially extensive oyster reefs, for example, *M. gigas* reefs in the central Wadden Sea, frictional wave energy dissipation can significantly impact the wave climate beyond the outlines of the reef's surface. It should, thus, be considered in regional modeling of the hydro- and morphodynamics.

The analysis in this work elucidates that lower densities of roughness elements imply higher wave energy dissipation. Oyster reefs surfaces are highly variable surfaces consisting of areas with densely packed individuals over clusters with lower abundances to bare sediment (Bungenstock et al., 2021; Markert, 2020). Hitzegrad, Brohmann et al. (2022) introduced seven structural classes of intertidal *M. gigas* reefs and identified associated topographical roughness parameters. Applying the results of this work implies that the more heterogeneous areas that are less densely settled and clustered (e.g., Transitional Zone, Cluster I, and Cluster II in Hitzegrad, Brohmann et al. (2022)) are most effective at attenuating waves and are subjected to the strongest forces induced by the bed shear stress. A study by McClenachan et al. (2020) confirms an increased cumulative effect of several small-scale restoration projects compared to their individual influence regarding shoreline protection.

While the present study highlights certain characteristics of ultra-rough oceanic surfaces by utilizing primitive, two-dimensional shapes, the bed roughness of in-situ or replicated ultra-rough oceanic surfaces comprises a number of additional characteristics that need to be considered. In contrast to the two-dimensional roughness elements investigated in this work, for example, oyster reef surfaces consist of highly three-dimensional agglomerations of oyster individuals. The surfaces vary in abundance of individuals, as well as the individuals' size, the shell morphology, and their orientation (Hitzegrad, Brohmann et al., 2022; Markert, 2020). Furthermore, the shaping of the shell edge depends on oyster species contributing to the complexity of the bed roughness (Gosling, 2015). Interactions between hydrodynamic conditions and directional features of oysters and clusters must be considered (Frey et al., 1987; Grinnell, 1974; Harzhauser et al., 2015). Hence, to provide realistic estimates of wave attenuation due to bed friction for oyster reefs or other ultra-rough oceanic

surfaces, in-situ measurements (similar to, e.g., Lowe et al. (2005) for coral reefs; Paul and Amos (2011) for seagrass meadows; or Donker et al. (2013) for mussel beds) or laboratory investigations utilizing surrogate models that comprise additional three-dimensional topographical characteristics typically linked to the hydraulic roughness (e.g., total roughness length k_t, abundance, higher statistical moments, and parameters considering clustering; compare Chung et al. (2021)) are necessary. From such additional analysis, canopy theory can be applied for an improved comparison to existing studies on ultra-rough oceanic surfaces, and hydraulic roughness parameters can be determined, which are necessary to improve the design of oyster reef structures for coastal protection and realistically predict hydro- and morphodynamics in local or regional models. Nonetheless, the results of this study illustrate that, even in a simplified two-dimensional setup, the shape of the roughness elements in an oceanic surface significantly influences the frictional wave energy dissipation and turbulence production.

In the present study, wave energy dissipation due to frictional dissipation has been considered in isolation. Under natural conditions, the transmitted wave energy is also influenced by wave attenuation due to wave breaking and reflection with varying influence depending on, for example, oyster species and seabed morphology (compare Figure 2), which should be considered in future investigations.

5. Conclusions

The main objective of this work was to investigate the sharpness of roughness elements of ultra-rough oceanic surfaces, for example, oyster reefs, as nucleation for wave attenuation effects. Six ultra-rough bed surface surrogates with varying sharpness of the roughness elements, sharp-edged (*lamella*), bluntly-shaped (*semicircle*), and combinations thereof (*mix*), have been subjected to regular waves with varying near-bed horizontal wave excursion amplitudes. The main conclusions of this study can be summarized as follows.

- Bed surfaces with sharp-edged roughness elements induce significantly stronger wave attenuation than bed surfaces with bluntly-shaped roughness elements. The shape of the elements below the edge has a subordinate influence. This observation confirms the hypothesis that strong vortices originate from the sharp edges, inducing a significant increase in friction when waves propagate over such surfaces.
- The highest bed shear stresses and hydraulic roughness lengths are generated for moderate near-bed horizontal wave excursion and wave orbital horizontal velocity amplitudes. It is suggested that the turbulence production reaches a threshold due to non-linear effects caused by increasing near-bed wave orbital horizontal velocity amplitude and relative roughness density, similar to effects found for increasing density of submerged canopies.
- The TKE method underestimates the frictional energy dissipation compared to the EB method for the bed surfaces with sharp-edged roughness elements. It is concluded that the TKE method does not capture the form-induced, dispersive stresses resulting from the separation and reattachment of the mean flow from the highly heterogeneous bed surfaces. Spatial- and phase-averaged velocity profiles are required to adequately capture the bed shear stresses. Furthermore, the study proposes an engineering approach to determine the relevant stress terms to improve the accuracy of estimating bed shear stresses in oscillatory flow over such complex bed configurations.
- Regarding natural ultra-rough oceanic bed surfaces, the results of this study imply that sharp-edged elements, such as oyster shells, are highly beneficial for wave energy dissipation. Hence, regional hydro-and morphodynamic numerical models should include the increased roughness for accurate estimations of wave attenuations. Furthermore, design strategies to include ultra-rough bed surfaces, for example, oyster reefs, as NbS for coastal protection, should be optimized based on the interaction length between waves and bed surfaces.

Appendix A: Sensitivity Study of the Turbulence Measurements

Figure A1 illustrates the sensitivity study performed to verify the robustness of the turbulence statistics of the VP measurements.
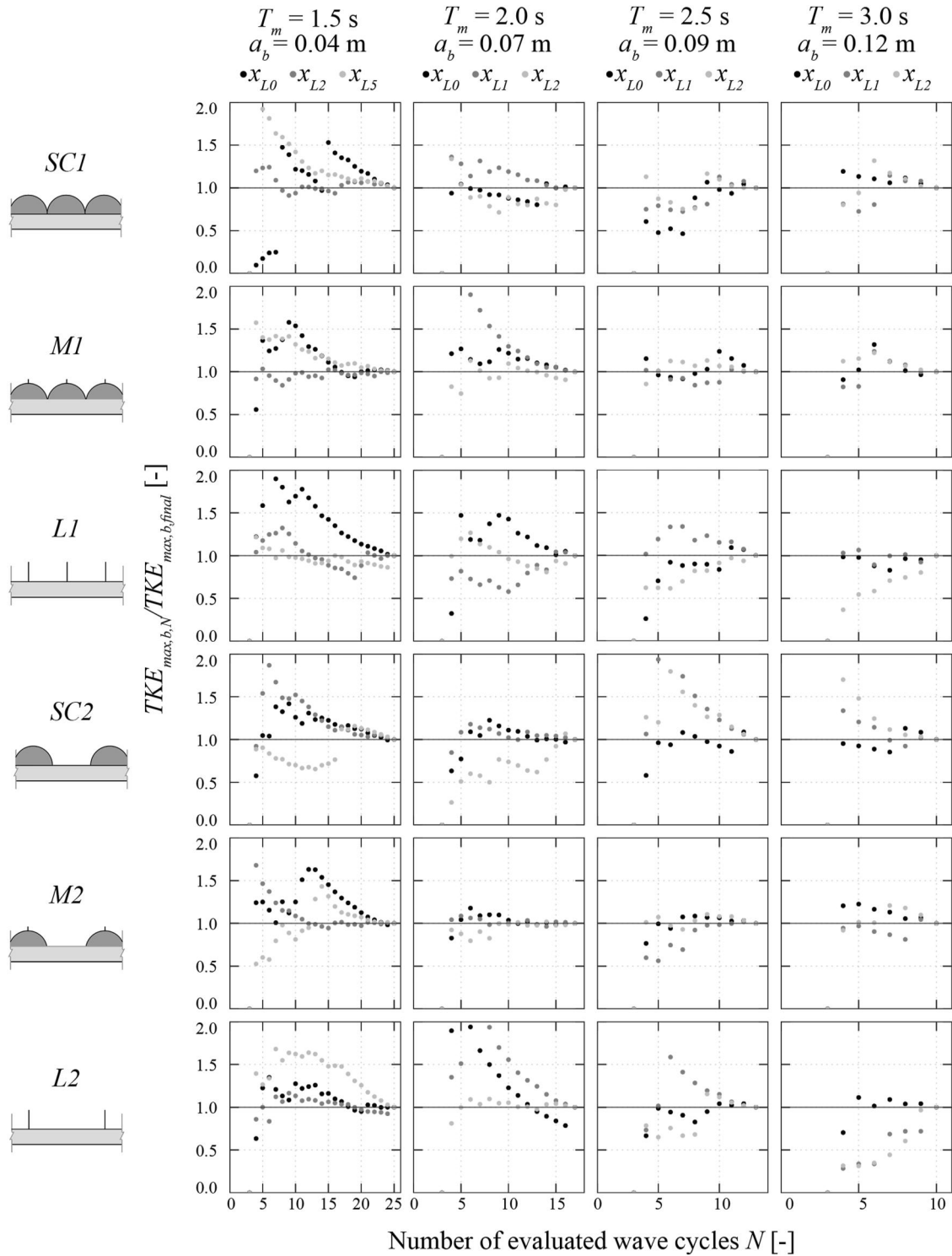
Figure A1. Sensitivity study comparing the maximum near-bed turbulent kinetic energy $TKE_{max,b,N}$ resulting from the evaluation of N wave cycles to the final $TKE_{max,b,final}$. Records are sorted by bed surface configurations (*SC1*: *semicircle 1, M1*: *mix 1, L1*: *lamella 1, SC2*: *semicircle 2, M2*: *mix 2, L2*: *lamella 2*) and hydrodynamic cases (mean wave period T_m and near-bed horizontal wave excursion amplitudes a_b). The black, dark gray, and light gray dots illustrate the records at x_{L0}, x_{L2}, and x_{L5} for $T_m = 1.5$ s, and at x_{L0}, x_{L1}, and x_{L2} for $T_m = 2.0$; 2.5; 3.0 s, respectively. Note that the gradient filter (see Section 3.2) was not implemented in the convergence study.

Appendix B: Near-Bed Horizontal Velocity and Maximum Turbulent Kinetic Energy for Positions x_{L1}, x_{L2}, and x_{L5}

Figure B1 illustrates the spatial and temporal distributions of the phase-averaged horizontal velocity $\tilde{u}$ and the turbulent kinetic energy TKE for positions x_{1L}, x_{2L}, and x_{5L}. Figure B2 illustrates the vertical distribution of the maximum positive and negative phase-averaged horizon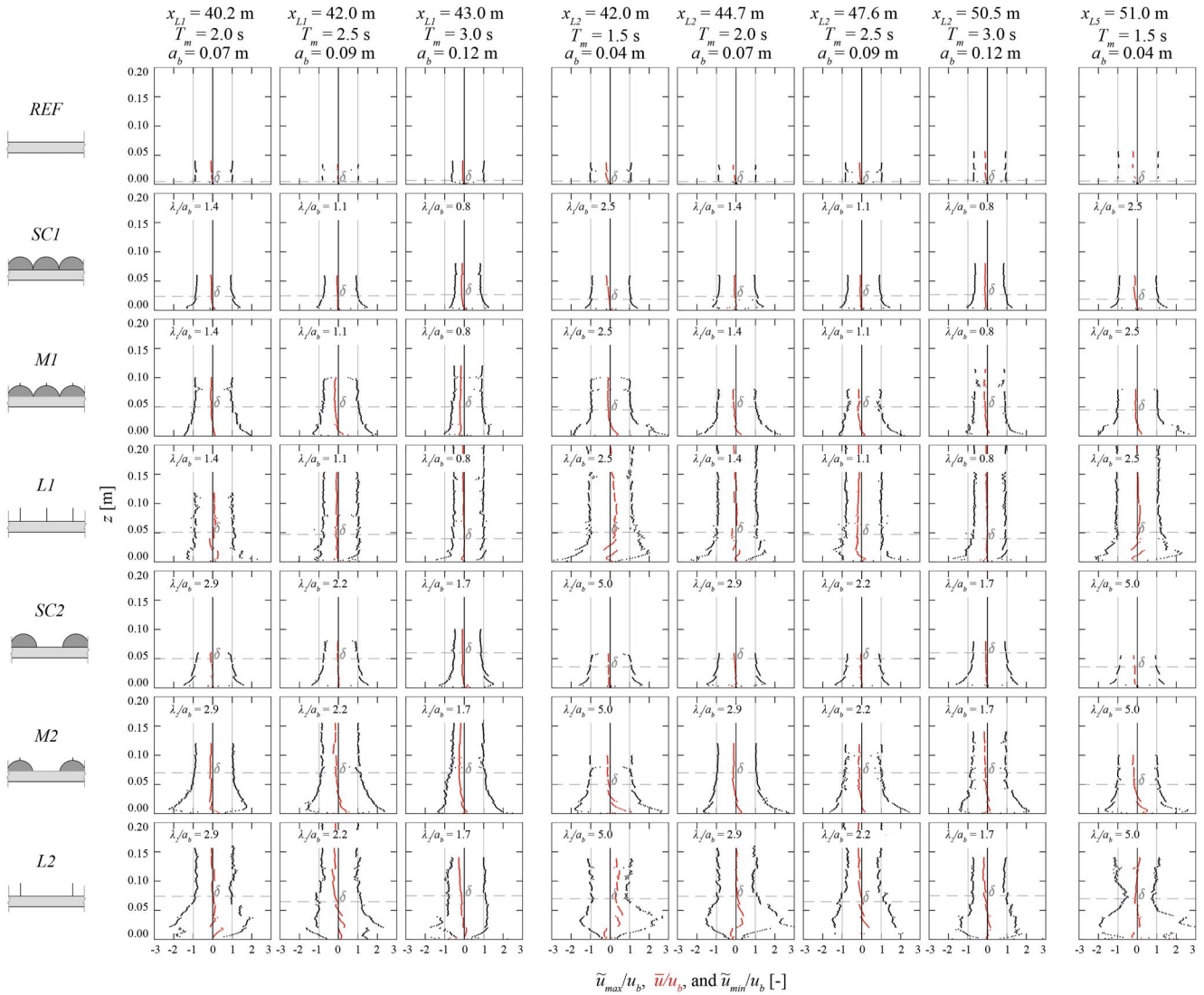tal velocity amplitudes, $\tilde{u}_{max}$ and $\tilde{u}_{min}$ normalized by the maximum near-bed wave orbital horizontal velocity amplitude u_b, for positions x_{1L}, x_{2L}, and x_{5L}. Figure B3 illustrates the maximum turbulent kinetic energy TKE_{max} normalized by the square of the maximum near-bed wave orbital horizontal velocity amplitude u_b^2 for the near the bed region for positions x_{1L}, x_{2L}, and x_{5L}.

Figure B1. Spatial (i.e., vertical) and temporal distributions of the phase-averaged horizontal orbital velocity $\tilde{u}$ [m/s] and the turbulent kinetic energy TKE [m²/s²] over the height z [m] in the near-bed region and a dimensionless wave cycle t/T_m [-]. Records at the positions x_{L1}, x_{L2}, x_{L5} are shown (Position x_{L0} in Figure 5), sorted by bed surface configurations (SC1: *semicircle 1, M1: mix 1, L1: lamella 1, SC2: semicircle 2, M2: mix 2, L2: lamella 2*) and hydrodynamic cases (mean wave period T_m and near-bed horizontal wave excursion amplitudes a_b). Parameter z is the height above the peak of the roughness elements or the bed surface (case *REF*), t is the time step, and λ is the spacing between roughness elements. Color scales: $\tilde{u}$: red to blue; TKE: yellow to green (Crameri, 2018); white areas: data was deleted by filtering or not recorded.

Figure B2. Vertical distribution of the maximum positive and negative phase-averaged horizontal orbital velocity amplitudes normalized by the maximum near-bed wave orbital horizontal velocity amplitude, $\tilde{u}_{max}/u_b$ and $\tilde{u}_{min}/u_b$ [-] (black, dotted lines), the normalized theoretical maximum positive and negative horizontal velocity amplitudes according to St second-order wave theory, $u_{Stokes,max}/u_b$ and $u_{Stokes,min}/u_b$, [-] (gray, solid line), and the normalized time-averaged horizontal velocity $\overline{u}/u_b$ [-] (red, dotted line) over the height z [m] in the near-bed region. Records at the positions x_{L1}, x_{L2}, x_{L5} are shown (Position x_{L0} in Figure 6), sorted bed surface configurations (*SC1*: s*emicircle 1, M1*: *mix 1*, *L1*: *lamella 1*, *SC2*: s*emicircle 2*, *M2*: *mix 2*, *L2*: *lamella 2*) and hydrodynamic cases (mean wave period T_m and near-bed horizontal wave excursion amplitudes a_b). The parameter λ is the spacing between roughness elements. The horizontal, dashed gray lines mark the thickness of the boundary layer δ, visually determined.
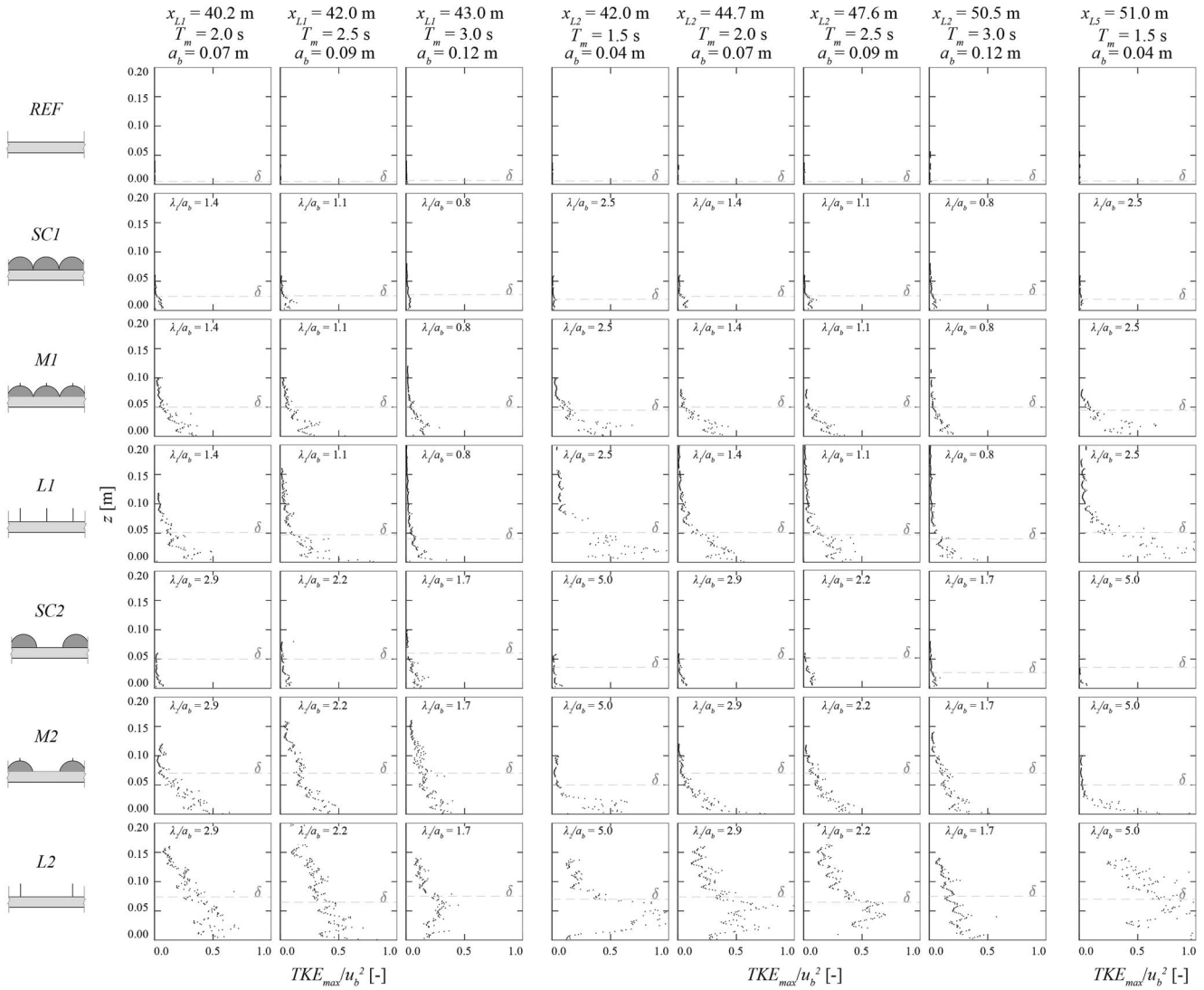
Figure B3. Vertical distribution of the maximum turbulent kinetic energy normalized by the square of the maximum near-bed wave orbital horizontal velocity amplitude TKE_{max}/u_b^2 [-] for the near the bed region over the height z [m]. Records at the positions x_{L1}, x_{L2}, x_{L5} are shown (Position x_{L0} in Figure 7), sorted by bed surface configurations (*SC1*: *semicircle 1*, *M1*: *mix 1*, *L1*: *lamella 1*, *SC2*: *semicircle 2*, *M2*: *mix 2*, *L2*: *lamella 2*) and hydrodynamic cases (wave period *T* and near-bed horizontal wave excursion amplitudes a_b). The parameter λ is the spacing between roughness elements. The horizontal, dashed gray lines mark the thickness of the boundary layer δ, visually determined.

Appendix C: Quantification of the Experimental Results

Table C1 and Table C2 summarize the experimental results of the EB and the TKE methods.

Table C1

Quantification of the Experimental Results by the Energy Balance Method Sorted by Bed Surface Configurations (SC1: Semicircle 1, M1: Mix 1, L1: Lamella 1, SC2: Semicircle 2, M2: Mix 2, L2: Lamella 2) and Hydrodynamic Cases (Mean Wave Period T_m and Near-Bed Horizontal Wave Excursion Amplitudes a_b)

	T_m [s]	a_b [m]	λ/a_b [-]	K_t [-]	f_w [-]	k_w [m]	$\tau_{w,max}$ [N/m^2]	Re [-]
SC1	1.5	0.04	2.5	0.99	0.042 ± 0.021	0.005 ± 0.003	0.80 ± 0.41	7.44 · 10^3
	2.0	0.07	1.4	0.97	0.049 ± 0.008	0.011 ± 0.002	1.73 ± 0.27	1.85 · 10^4
	2.5	0.09	1.1	0.98	0.040 ± 0.018	0.013 ± 0.008	1.93 ± 0.84	3.09 · 10^4
	3.0	0.12	0.8	1.01	0.003 ± 0.007	0.001 ± 0.002	0.23 ± 0.51	5.80 · 10^4
M1	1.5	0.04	2.5	0.91	0.477 ± 0.023	0.064 ± 0.002	7.62 ± 0.33	6.23 · 10^3
	2.0	0.07	1.4	0.88	0.329 ± 0.007	0.085 ± 0.002	10.08 ± 0.27	1.59 · 10^4
	2.5	0.09	1.1	0.90	0.204 ± 0.013	0.077 ± 0.005	7.96 ± 0.46	2.53 · 10^4
	3.0	0.12	0.8	0.95	0.081 ± 0.010	0.042 ± 0.006	4.79 ± 0.60	4.62 · 10^4
L1	1.5	0.04	2.5	0.86	0.773 ± 0.031	0.092 ± 0.002	11.85 ± 0.35	5.97 · 10^3
	2.0	0.07	1.4	0.83	0.420 ± 0.021	0.105 ± 0.005	12.71 ± 0.75	1.57 · 10^4
	2.5	0.09	1.1	0.88	0.240 ± 0.010	0.088 ± 0.004	8.98 ± 0.48	2.43 · 10^4
	3.0	0.12	0.8	0.92	0.104 ± 0.011	0.057 ± 0.007	6.28 ± 0.78	4.69 · 10^4
SC2	1.5	0.04	5.0	0.99	0.031 ± 0.034	0.004 ± 0.006	0.62 ± 0.69	7.56 · 10^3
	2.0	0.07	2.9	0.97	0.048 ± 0.009	0.011 ± 0.003	1.77 ± 0.34	1.91 · 10^4
	2.5	0.09	2.2	0.98	0.042 ± 0.013	0.014 ± 0.006	2.00 ± 0.61	3.10 · 10^4
	3.0	0.12	1.7	0.95	0.063 ± 0.009	0.036 ± 0.006	4.99 ± 0.75	6.20 · 10^4
M2	1.5	0.04	5.0	0.94	0.319 ± 0.025	0.045 ± 0.003	5.19 ± 0.44	6.33 · 10^3
	2.0	0.07	2.9	0.88	0.345 ± 0.005	0.089 ± 0.001	10.68 ± 0.15	1.61 · 10^4
	2.5	0.09	2.2	0.85	0.290 ± 0.012	0.106 ± 0.002	11.07 ± 0.22	2.48 · 10^4
	3.0	0.12	1.7	0.86	0.204 ± 0.016	0.114 ± 0.009	12.18 ± 1.05	4.65 · 10^4
L2	1.5	0.04	5.0	0.81	0.944 ± 0.028	0.111 ± 0.002	15.55 ± 0.43	6.41 · 10^3
	2.0	0.07	2.9	0.76	0.615 ± 0.011	0.146 ± 0.001	19.05 ± 0.29	1.61 · 10^4
	2.5	0.09	2.2	0.77	0.424 ± 0.012	0.151 ± 0.002	16.82 ± 0.23	2.57 · 10^4
	3.0	0.12	1.7	0.85	0.213 ± 0.006	0.121 ± 0.004	12.99 ± 0.55	4.77 · 10^4

Note. The parameter λ is the spacing between roughness elements, K_t is the transmission coefficient, f_w is the wave friction factor, k_w is the hydraulic roughness length, $\tau_{w,max}$ is the maximum bed shear stress, and Re is the Reynolds number.

Table C2
Quantification of the Experimental Results of the Turbulent Kinetic Energy Method Sorted by Bed Surface Configurations (SC1: Semicircle 1, M1: Mix 1, L1: Lamella 1, SC2: Semicircle 2, M2: Mix 2, L2: Lamella 2) and Hydrodynamic Cases (Mean Wave Period T_m and Near-Bed Horizontal Wave Excursion Amplitudes a_b)

	T_m [s]	a_b [m]	λ/a_b [-]	δ [m]	$TKE_{max,b}$ [m^2/s^2]	f_w [-]	k_w [m]	$\tau_{w,max}$ [N/m^2]	Re [-]
REF	1.5	0.04	-	0.006	0.000 ± 0.000	0.002 ± 0.000	0.000 ± 0.000	0.02 ± 0.00	$7.44 \cdot 10^3$
	2.0	0.07	-	0.005	0.000 ± 0.000	0.002 ± 0.000	0.000 ± 0.000	0.04 ± 0.01	$1.08 \cdot 10^4$
	2.5	0.09	-	0.005	0.000 ± 0.000	0.003 ± 0.001	0.000 ± 0.000	0.05 ± 0.04	$1.68 \cdot 10^4$
	3.0	0.12	-	0.007	0.001 ± 0.000	0.003 ± 0.001	0.000 ± 0.000	0.13 ± 0.05	$3.10 \cdot 10^4$
SC1	1.5	0.04	2.5	0.019	0.001 ± 0.000	0.010 ± 0.000	0.000 ± 0.000	0.15 ± 0.01	$5.69 \cdot 10^3$
	2.0	0.07	1.4	0.024	0.005 ± 0.001	0.032 ± 0.008	0.003 ± 0.001	0.88 ± 0.18	$1.43 \cdot 10^4$
	2.5	0.09	1.1	0.025	0.007 ± 0.001	0.036 ± 0.007	0.005 ± 0.002	1.30 ± 0.25	$2.33 \cdot 10^4$
	3.0	0.12	0.8	0.027	0.006 ± 0.002	0.021 ± 0.007	0.003 ± 0.002	1.14 ± 0.31	$4.21 \cdot 10^4$
M1	1.5	0.04	2.5	0.045	0.014 ± 0.002	0.235 ± 0.010	0.019 ± 0.001	2.65 ± 0.35	$4.39 \cdot 10^3$
	2.0	0.07	1.4	0.050	0.014 ± 0.001	0.127 ± 0.027	0.018 ± 0.003	2.72 ± 0.27	$1.13 \cdot 10^4$
	2.5	0.09	1.1	0.050	0.019 ± 0.003	0.129 ± 0.022	0.026 ± 0.005	3.53 ± 0.62	$1.79 \cdot 10^4$
	3.0	0.12	0.8	0.050	0.017 ± 0.004	0.072 ± 0.014	0.019 ± 0.005	3.17 ± 0.73	$3.42 \cdot 10^4$
L1	1.5	0.04	2.5	0.051	0.022 ± 0.001	0.407 ± 0.107	0.031 ± 0.003	4.10 ± 0.15	$4.09 \cdot 10^3$
	2.0	0.07	1.4	0.051	0.025 ± 0.009	0.219 ± 0.048	0.033 ± 0.010	4.76 ± 1.72	$1.11 \cdot 10^4$
	2.5	0.09	1.1	0.047	0.030 ± 0.010	0.211 ± 0.063	0.044 ± 0.015	5.67 ± 1.99	$1.73 \cdot 10^4$
	3.0	0.12	0.8	0.040	0.023 ± 0.004	0.102 ± 0.030	0.029 ± 0.009	4.36 ± 0.77	$3.42 \cdot 10^4$
SC2	1.5	0.04	5.0	0.036	0.002 ± 0.000	0.026 ± 0.003	0.001 ± 0.000	0.40 ± 0.03	$6.01 \cdot 10^3$
	2.0	0.07	2.9	0.050	0.004 ± 0.001	0.031 ± 0.006	0.003 ± 0.001	0.84 ± 0.12	$1.42 \cdot 10^4$
	2.5	0.09	2.2	0.050	0.007 ± 0.000	0.035 ± 0.002	0.005 ± 0.000	1.30 ± 0.02	$2.46 \cdot 10^4$
	3.0	0.12	1.7	0.060	0.018 ± 0.003	0.068 ± 0.009	0.019 ± 0.003	3.50 ± 0.50	$4.08 \cdot 10^4$
M2	1.5	0.04	5.0	0.050	0.017 ± 0.003	0.276 ± 0.037	0.023 ± 0.004	3.17 ± 0.66	$4.45 \cdot 10^3$
	2.0	0.07	2.9	0.070	0.023 ± 0.003	0.210 ± 0.051	0.031 ± 0.006	4.43 ± 0.51	$1.12 \cdot 10^4$
	2.5	0.09	2.2	0.070	0.022 ± 0.006	0.167 ± 0.012	0.033 ± 0.006	4.21 ± 1.11	$1.62 \cdot 10^4$
	3.0	0.12	1.7	0.070	0.028 ± 0.002	0.142 ± 0.023	0.040 ± 0.004	5.23 ± 0.30	$2.92 \cdot 10^4$
L2	1.5	0.04	5.0	0.070	0.030 ± 0.008	0.568 ± 0.088	0.041 ± 0.006	5.70 ± 1.52	$3.95 \cdot 10^3$
	2.0	0.07	2.9	0.074	0.028 ± 0.004	0.280 ± 0.050	0.040 ± 0.003	5.41 ± 0.74	$1.04 \cdot 10^4$
	2.5	0.09	2.2	0.065	0.033 ± 0.010	0.269 ± 0.009	0.052 ± 0.008	6.31 ± 1.85	$1.53 \cdot 10^4$
	3.0	0.12	1.7	0.075	0.032 ± 0.003	0.159 ± 0.025	0.046 ± 0.003	6.01 ± 0.53	$3.04 \cdot 10^4$

Note. The parameter λ is the spacing between roughness elements, δ is the boundary layer height (visually determined), $TKE_{max,b}$ is the maximum turbulent kinetic energy, f_w is the wave friction factor, k_w is the hydraulic roughness length, $\tau_{w,max}$ is the maximum bed shear stress, and Re is the Reynolds number.

Appendix D: Double-Averaged Flow Parameters

Figure D1 shows the vertical distributions of the individual $\tilde{u}_{max}/u_b$, $\tilde{u}_{min}/u_b$, $\overline{u}/u_b$, and TKE_{max}/ub^2 at the four x_{L0}, $x_{L0,1}$, $x_{L0,2}$, $x_{L0,3}$, and the double averaged $\langle\tilde{u}\rangle_{max}/u_b$, $\langle\tilde{u}\rangle_{min}/u_b$, $\langle\overline{u}\rangle/u_b$, and $\langle TKE\rangle_{max}/u_b^2$. Table D1 summarizes the experimental results of the TKE-WKE method.
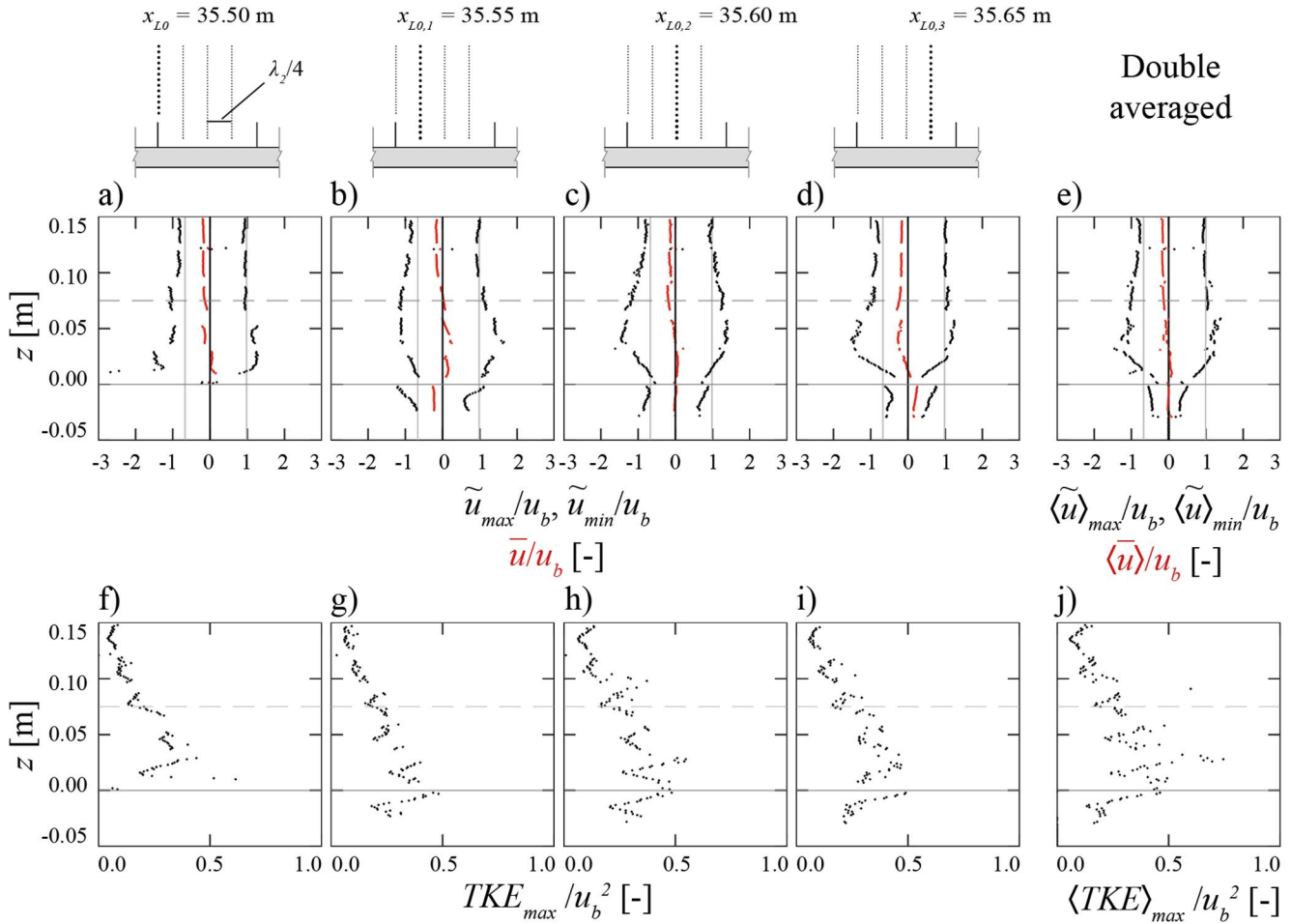
Figure D1. Visualization of the double-averaging, exemplarily for the case of $L2$ with $T_m = 3.0$ s and $a_b = 0.12$ m. (a)–(d) Vertical distribution of the maximum positive and negative phase-averaged horizontal orbital velocity amplitudes normalized by the maximum near-bed wave orbital horizontal velocity amplitude, $\tilde{u}_{max}/u_b$, $\tilde{u}_{min}/u_b$ (black, dotted lines) [-], and the normalized time-averaged horizontal velocity, $\overline{u}/u_b$ [-], (red, dotted line) over the height z [m] in the near-bed region measured at the four x-locations (a): x_{L0}, (b) $x_{L0,1}$, (b) $x_{L0,2}$, (b) $x_{L0,3}$), (e) Vertical distribution of the normalized maximum positive and negative spatial- and phase-averaged horizontal orbital velocity amplitudes $\langle\tilde{u}\rangle_{max}/u_b$, $\langle\tilde{u}\rangle_{min}/u_b$ (black, dotted lines) [-], and the normalized spatial- and time-averaged horizontal velocity $\langle\overline{u}\rangle/u_b$ [-] (red, dotted line) over the height z [m] in the near-bed region. The normalized theoretical maximum positive and negative horizontal velocity amplitudes according to St second-order wave theory, $u_{Stokes,max}/u_b$ and $u_{Stokes,min}/u_b$, [-] are shown with gray, solid lines. (f)–(i) Vertical distribution of the maximum turbulent kinetic energy normalized by the square of the maximum near-bed wave orbital horizontal velocity amplitude TKE_{max}/u_b^2 [-] over the height z [m] in the near-bed region measured at the four x locations (a): x_{L0}, (b) $x_{L0,1}$, (b) $x_{L0,2}$, (b) $x_{L0,3}$). (j) Vertical distribution of the normalized maximum double-averaged turbulent kinetic energy normalized by the square of the maximum near-bed wave orbital horizontal velocity amplitude $\langle TKE\rangle_{max}/u_b^2$ [-].

Table D1

Quantification of the Experimental Results of the TKE-WKE Method Sorted by Bed Surface Configurations (SC1: Semicircle 1, M1: Mix 1, L1: Lamella 1, SC2: Semicircle 2, M2: Mix 2, L2: Lamella 2) and Hydrodynamic Cases (Mean Wave Period T_m and Near-Bed Horizontal Wave Excursion Amplitudes a_b)

	T_m [s]	a_b [m]	λ/a_b [-]	$\langle TKE \rangle_{b,max}$ [-]	$\langle WKE \rangle_{b,max}$ [-]	$\tau_{w,max,\langle TKE \rangle + \langle WKE \rangle}$ [-]
SC1	2.0	0.07	1.4	0.005	0.006	2.13
	3.0	0.12	0.8	0.009	0.011	3.92
M1	2.0	0.07	1.4	0.022	0.012	6.49
	3.0	0.12	0.8	0.021	0.02	7.95
L1	2.0	0.07	1.4	0.026	0.018	8.35
	3.0	0.12	0.8	0.033	0.019	9.98
SC2	2.0	0.07	1.4	0.009	0.011	3.9
	3.0	0.12	0.8	0.015	0.021	6.73
M2	2.0	0.07	1.4	0.028	0.025	10.04
	3.0	0.12	0.8	0.036	0.033	13.1
L2	2.0	0.07	1.4	0.039	0.023	11.7
	3.0	0.12	0.8	0.059	0.021	15.22

Note. Where $\langle TKE \rangle_{b,max}$ is the maximum near-bed phase-averaged turbulent kinetic energy, and $\langle WKE \rangle_{b,max}$ is the maximum near-bed phase-averaged wake kinetic energy.

Conflict of Interest

The authors declare no conflicts of interest relevant to this study.

Data Availability Statement

The data used in this study can be accessed online at Hitzegrad, Köster, et al. (2022).

References

Abdolahpour, M., Ghisalberti, M., Lavery, P., & McMahon, K. (2017). Vertical mixing in coastal canopies. *Limnology & Oceanography*, *62*(1), 26–42. https://doi.org/10.1002/lno.10368

Agelinchaab, M., & Tachie, M. F. (2006). Open channel turbulent flow over hemispherical ribs. *International Journal of Heat and Fluid Flow*, *27*(6), 1010–1027. https://doi.org/10.1016/j.ijheatfluidflow.2006.03.001

Allen, R., & Webb, B. M. (2011). Determination of wave transmission coefficients for oyster shell bag breakwaters. In O. T. Magoon, R. M. Noble, D. D. Treadwell, & Y. C. Kim (Eds.), *Coastal engineering practice* (pp. 684–697). American Society of Civil Engineers. https://doi.org/10.1061/41190(422)57

Ardhuin, F., Herbers, T. H. C., & O'Reilly, W. C. (2001). A hybrid Eulerian–Lagrangian model for spectral wave evolution with application to bottom friction on the continental shelf. *Journal of Physical Oceanography*, *31*(6), 1498–1516. https://doi.org/10.1175/1520-0485(2001)031<1498:ahelmf>2.0.co;2

Bagherimiyab, F., & Lemmin, U. (2013). Shear velocity estimates in rough-bed open-channel flow. *Earth Surface Processes and Landforms*, *38*(14), 1714–1724. https://doi.org/10.1002/esp.3421

Bahr, L. M., & Lanier, W. P. (1981). *The ecology of intertidal oyster reefs of the South Atlantic coast: A community profile: FWS/OBS-81/15*. U.S. Fish and Wildlife Service, Office of Biological Services.

Battjes, J. A., & Janssen, J. P. F. M. (1978). Energy loss and set-up due to breaking of random waves. In *Coastal engineering 1978* (pp. 569–587). American Society of Civil Engineers. https://doi.org/10.1061/9780872621909.034

Belcher, S. E., Harman, I. N., & Finnigan, J. J. (2012). The wind in the willows: Flows in forest canopies in complex terrain. *Annual Review of Fluid Mechanics*, *44*(1), 479–504. https://doi.org/10.1146/annurev-fluid-120710-101036

Biron, P. M., Robson, C., Lapointe, M. F., & Gaskin, S. J. (2004). Comparing different methods of bed shear stress estimates in simple and complex flow fields. *Earth Surface Processes and Landforms*, *29*(11), 1403–1415. https://doi.org/10.1002/esp.1111

Borsje, B. W., Van Wesenbeeck, B. K., Dekker, F., Paalvast, P., Bouma, T. J., Van Katwijk, M. M., & De Vries, M. B. (2011). How ecological engineering can serve in coastal protection. *Ecological Engineering*, *37*(2), 113–122. https://doi.org/10.1016/j.ecoleng.2010.11.027

Bouma, T. J., Van Belzen, J., Balke, T., Zhu, Z., Airoldi, L., Blight, A. J., et al. (2014). Identifying knowledge gaps hampering application of intertidal habitats in coastal protection: Opportunities & steps to take. *Coastal Engineering*, *87*, 147–157. https://doi.org/10.1016/j.coastaleng.2013.11.014

Brevik, I., & Bjørn, A. (1980). Flume experiment on waves and currents. I. Rippled bed. *Coastal Engineering*, *3*, 149–177. https://doi.org/10.1016/0378-3839(79)90019-X

Britter, R. E., & Hanna, S. R. (2003). Flow and dispersion in urban areas. *Annual Review of Fluid Mechanics*, *35*(1), 469–496. https://doi.org/10.1146/annurev.fluid.35.101101.161147

Buckley, M. L., Lowe, R. J., Hansen, J. E., Van Dongeren, A. R., Pomeroy, A., Storlazzi, C. D., et al. (2022). Wave-driven hydrodynamic processes over fringing reefs with varying slopes, depths, and roughness: Implications for coastal protection. *Journal of Geophysical Research: Oceans*, *127*(11). https://doi.org/10.1029/2022JC018857

Bungenstock, F., Hertweck, G., Hochstein, M. L., & Wehrmann, A. (2021). Distribution pattern and controls of biosedimentary facies in backbarrier tidal flats of the central Wadden Sea (North Sea). *Journal of Applied and Regional Geology*, *172*(4), 409–428. https://doi.org/10.1127/zdgg/2021/0248

Butterworth, S. (1930). On the theory of filter amplifiers. *Experimental Wireless and the Wireless Engineer*, *7*, 536–541.

Choe, B.-H., & Kim, D. (2019). SAR remote sensing of intertidal flats in Korea. In V. Barale & M. Gade (Eds.), *Remote sensing of the Asian seas* (pp. 237–250). Springer International Publishing. https://doi.org/10.1007/978-3-319-94067-0_13

Choe, B.-H., Kim, D., Hwang, J.-H., Oh, Y., & Moon, W. M. (2012). Detection of oyster habitat in tidal flats using multi-frequency polarimetric SAR data. *Estuarine, Coastal and Shelf Science*, *97*, 28–37. https://doi.org/10.1016/j.ecss.2011.11.007

Chowdhury, M. S. N., Walles, B., Sharifuzzaman, S. M., Shahadat Hossain, M., Ysebaert, T., & Smaal, A. C. (2019). Oyster breakwater reefs promote adjacent mudflat stability and salt marsh growth in a monsoon dominated subtropical coast. *Scientific Reports*, *9*(1), 1–12. https://doi.org/10.1038/s41598-019-44925-6

Chung, D., Hutchins, N., Schultz, M. P., & Flack, K. A. (2021). Predicting the drag of rough surfaces. *Annual Review of Fluid Mechanics*, *53*(1), 439–471. https://doi.org/10.1146/annurev-fluid-062520-115127

Coleman, S. E., Nikora, V. I., & Schlicke, T. (2008). Spatially-averaged oscillatory flow over a rough bed. *Acta Geophysica*, *56*(3), 698–733. https://doi.org/10.2478/s11600-008-0016-z

Conde-Frias, M., Ghisalberti, M., Lowe, R. J., Abdolahpour, M., & Etminan, V. (2023). The near-bed flow structure and bed shear stresses within emergent vegetation. *Water Resources Research*, *59*(4). https://doi.org/10.1029/2022WR032499

Crameri, F. (2018). Geodynamic diagnostics, scientific visualisation and StagLab 3.0. *Geoscientific Model Development*, *11*(6), 2541–2562. https://doi.org/10.5194/gmd-11-2541-2018

Dade, W. B., Hogg, A. J., & Boudreau, B. P. (2001). Physics of flow above the sediment water interface. In B. P. Boudreau (Ed.), *The Benthic boundary layer: Transport processes and biogeochemistry* (pp. 4–43). Oxford University Press. https://doi.org/10.1093/oso/9780195118810.003.0002

Dame, R. F. (2016). *Ecology of marine bivalves: An ecosystem approach*. CRC Press.

Dean, R. G., & Dalrymple, R. A. (1991). Water wave mechanics for engineers and scientists. *World Scientific*, *2*.

Dixen, M., Hatipoglu, F., Sumer, B. M., & Fredsøe, J. (2008). Wave boundary layer over a stone-covered bed. *Coastal Engineering*, *55*(1), 1–20. https://doi.org/10.1016/j.coastaleng.2007.06.005

Dong, G., Gao, X., Ma, X., & Ma, Y. (2020). Energy properties of regular water waves over horizontal bottom with increasing nonlinearity. *Ocean Engineering*, *218*, 108159. https://doi.org/10.1016/j.oceaneng.2020.108159

Donker, J., Van Der Vegt, M., & Hoekstra, P. (2013). Wave forcing over an intertidal mussel bed. *Journal of Sea Research*, *82*, 54–66. https://doi.org/10.1016/j.seares.2012.08.010

Dunbar, D., Van Der A, D. A., Scandura, P., & O'Donoghue, T. (2023). An experimental and numerical study of turbulent oscillatory flow over an irregular rough wall. *Journal of Fluid Mechanics*, *955*, A33. https://doi.org/10.1017/jfm.2022.1090

Finnigan, J. J. (2000). Turbulence in plant canopies. *Annual Review of Fluid Mechanics*, *32*(1), 519–571. https://doi.org/10.1146/annurev.fluid.32.1.519

Fodrie, F. J., Rodriguez, A. B., Gittman, R. K., Grabowski, J. H., Lindquist, N. L., Peterson, C. H., et al. (2017). Oyster reefs as carbon sources and sinks. *Proceedings of the Royal Society B: Biological Sciences*, *284*(1859), 1–9. https://doi.org/10.1098/rspb.2017.0891

Folmer, E. O., Büttger, H., Herlyn, M., Markert, A., Millat, G., Troost, K., & Wehrmann, A. (2017). In S. Kloepper (Ed.), *Beds of blue mussels and Pacific oysters. In: Wadden sea quality status 2017*. Common Wadden Sea Secretary.

Folmer, E. O., Drent, J., Troost, K., Büttger, H., Dankers, N., Jansen, J., et al. (2014). Large-scale spatial dynamics of intertidal mussel (*Mytilus edulis* L.) bed coverage in the German and Dutch Wadden Sea. *Ecosystems*, *17*(3), 550–566. https://doi.org/10.1007/s10021-013-9742-4

Fredsøe, J., Andersen, K. H., & Mutlu Sumer, B. (1999). Wave plus current over a ripple-covered bed. *Coastal Engineering*, *38*(4), 177–221. https://doi.org/10.1016/S0378-3839(99)00047-2

Fredsøe, J., & Deigaard, R. (1992). *Mechanics of coastal sediment transport. Advanced series on ocean engineering. Vol. 3*. World Scientific.

Frey, R. W., Basan, P. B., & Smith, J. M. (1987). Rheotaxis and distribution of oysters and mussels, Georgia tidal creeks and salt marshes, U.S.A. *Palaeogeography, Palaeoclimatology, Palaeoecology*, *61*, 1–16. https://doi.org/10.1016/0031-0182(87)90038-1

Fuhrman, D. R., Schløer, S., & Sterner, J. (2013). RANS-based simulation of turbulent wave boundary layer and sheet-flow sediment transport processes. *Coastal Engineering*, *73*, 151–166. https://doi.org/10.1016/j.coastaleng.2012.11.001

García-March, J. R., Pérez-Rojas, L., & García-Carrascosa, A. M. (2007). Influence of hydrodynamic forces on population structure of *Pinna nobilis* L., 1758 (Mollusca: Bivalvia): The critical combination of drag force, water depth, shell size and orientation. *Journal of Experimental Marine Biology and Ecology*, *342*(2), 202–212. https://doi.org/10.1016/j.jembe.2006.09.007

Garvis, S. K. (2012). *Quantifying the impacts of oyster reef restoration on oyster coverage, wave energy dissipation and seagrass recruitment in Mosquito Lagoon, Florida (Master's thesis)*. University of Central Florida, Orlando, FL. Retrieved from https://stars.library.ucf.edu/etd/2284/

Ghodke, C. D., & Apte, S. V. (2016). DNS study of particle-bed–turbulence interactions in an oscillatory wall-bounded flow. *Journal of Fluid Mechanics*, *792*, 232–251. https://doi.org/10.1017/jfm.2016.85

Ghodke, C. D., & Apte, S. V. (2018). Roughness effects on the second-order turbulence statistics in oscillatory flows. *Computers & Fluids*, *162*, 160–170. https://doi.org/10.1016/j.compfluid.2017.09.021

Giménez-Curto, L. A., & Lera, M. A. C. (1996). Oscillating turbulent flow over very rough surfaces. *Journal of Geophysical Research*, *101*(C9), 20745–20758. https://doi.org/10.1029/96JC01824

Goring, D. G., & Nikora, V. I. (2002). Despiking acoustic doppler velocimeter data. *Journal of Hydraulic Engineering*, *128*(1), 117–126. https://doi.org/10.1061/(asce)0733-9429(2002)

Gormus, T. (2021). Zero up/down crossing method for waves. Retrieved from https://github.com/TahsinGormus/coastalengtoolbox/releases/tag/1.0.0.1

Gosling, E. M. (2015). *Marine bivalve molluscs* (2nd ed.). Wiley-Blackwell.

Grabowski, J. H., Brumbaugh, R. D., Conrad, R. F., Keeler, A. G., Opaluch, J. J., Peterson, C. H., et al. (2012). Economic valuation of ecosystem services provided by oyster reefs. *BioScience*, *62*(10), 900–909. https://doi.org/10.1525/bio.2012.62.10.10

Grinnell, R. S. (1974). Vertical orientation of shells on some Florida oyster reefs. *Journal of Sedimentary Research*, *44*, 116–122. https://doi.org/10.1306/74D72996-2B21-11D7-8648000102C1865D

Gutiérrez, J. L., Jones, C. G., Strayer, D. L., & Iribarne, O. O. (2003). Mollusks as ecosystem engineers: The role of shell production in aquatic habitats. *Oikos*, *101*(1), 79–90. https://doi.org/10.1034/j.1600-0706.2003.12322.x

Harris, D. L., Rovere, A., Casella, E., Power, H., Canavesio, R., Collin, A., et al. (2018). Coral reef structural complexity provides important coastal protection from waves under rising sea levels. *Science Advances*, *4*(2), eaao4350. https://doi.org/10.1126/sciadv.aao4350

Harzhauser, M., Djuricic, A., Mandic, O., Zuschin, M., Dorninger, P., Nothegger, C., et al. (2015). Disentangling the history of complex multi-phased shell beds based on the analysis of 3D point cloud data. *Palaeogeography, Palaeoclimatology, Palaeoecology*, *437*, 165–180. https://doi.org/10.1016/j.palaeo.2015.07.038

Hayward, P. J. & Ryland, J. S. (Eds.) (2017)., *Handbook of the marine fauna of North-West Europe* (2nd ed.). Oxford University Press.

He, S., Liu, H., & Shen, L. (2022). Simulation-based study with turbulent aquatic canopy flows with flexible stems. *Journal of Fluid Mechanics*, *947*, A33. https://doi.org/10.1017/jfm.2022.655

Hitzegrad, J., Brohmann, L., Pfennings, K., Hoffmann, T. K., Eilrich, A. K., Paul, M., et al. (2022). Oyster reef surfaces in the central Wadden Sea: Intra-reef classification and comprehensive statistical description. *Frontiers in Marine Science*, *9*. https://doi.org/10.3389/fmars.2022.808018

Hitzegrad, J., Köster, S., Windt, C., & Goseberg, N. (2022). Water surface elevations and near-bed velocity measurements over ultra-rough bed surfaces subjected to regular waves [Dataset]. https://doi.org/10.24355/dbbs.084-202209221223-0

Huang, Z.-C., Lenain, L., Melville, W. K., Middleton, J. H., Reineman, B., Statom, N., & McCabe, R. M. (2012). Dissipation of wave energy and turbulence in a shallow coral reef lagoon. *Journal of Geophysical Research*, *117*(C3). https://doi.org/10.1029/2011jc007202

Hunt, J. N. (1952). Amortissement par Viscosité de la Houle Sur un Fond Incliné Dans un Canal de Largeur Finie - Viscous damping of waves on an inclined bed in a channel of finite width. *La Houille Blanche*, *38*(6), 836–842. https://doi.org/10.1051/lhb/1952054

Jiang, B., Zhang, H., You, T., Sun, Y., Fu, C., Liao, W., & Cai, F. (2022). Experimental study on the effect of an oyster reef on the nonlinear characteristics of irregular waves. *Frontiers in Marine Science*, *9*. https://doi.org/10.3389/fmars.2022.1096497

Jiménez, J. (2004). Turbulent flows over rough walls. *Annual Review of Fluid Mechanics*, *36*(1), 173–196. https://doi.org/10.1146/annurev.fluid.36.050802.122103

Jones, C. G., Lawton, J. H., & Shachak, M. (1994). Organisms as ecosystem engineers. *Oikos*, *69*(3), 373–386. https://doi.org/10.2307/3545850

Jonsson, I. G. (1966). Wave boundary layers and friction factors. *Coastal Engineering Proceedings*, *1*(10), 9. https://doi.org/10.9753/icce.v10.9

Kajiura, K. (1968). A model of the bottom boundary layer in water waves. *Bulletin of the Earthquake Research Institute*, *46*(5), 75–123.

Kamphuis, J. W. (1975). Friction factor under oscillatory waves. *Journal of the Waterways, Harbors and Coastal Engineering Division*, *101*(2), 135–144. https://doi.org/10.1061/AWHCAR.0000276

Kennedy, V. S. (Ed.) (1996)., *A Maryland sea grant book. The eastern oyster: Crassostrea virginica*. Maryland Sea Grant College.

Kim, K.-L., & Ryu, J.-H. (2020). Mapping oyster reef distribution using Kompsat-2/3 and linear spectral unmixing Algorithm - A case study at Hwangdo Tidal Flat. *Journal of Coastal Research*, *102*(sp1). https://doi.org/10.2112/SI102-030.1

Kim, S.-C., Friedrichs, C. T., Maa, J. P.-Y., & Wright, L. D. (2000). Estimating bottom stress in tidal boundary layer from acoustic doppler velocimeter data. *Journal of Hydraulic Engineering*, *126*(6), 399–406. https://doi.org/10.1061/(asce)0733-9429(2000)

Kitsikoudis, V., Kibler, K. M., & Walters, L. J. (2020). In-situ measurements of turbulent flow over intertidal natural and degraded oyster reefs in an estuarine lagoon. *Ecological Engineering*, *143*, 105688. https://doi.org/10.1016/j.ecoleng.2019.105688

Koca, K., Noss, C., Anlanger, C., Brand, A., & Lorke, A. (2017). Performance of the Vectrino Profiler at the sediment–water interface. *Journal of Hydraulic Research*, *55*(4), 573–581. https://doi.org/10.1080/00221686.2016.1275049

Lacey, J., Duguay, J., & MacVicar, B. (2018). Comparison of velocity and turbulence profiles obtained with a Vectrino Profiler and PIV. *E3S Web of Conferences*, *40*, 5070. https://doi.org/10.1051/e3sconf/20184005070

Lacy, J. R., & MacVean, L. J. (2016). Wave attenuation in the shallows of San Francisco Bay. *Coastal Engineering*, *114*, 159–168. https://doi.org/10.1016/j.coastaleng.2016.03.008

Le Méhauté, B. (1976). *An introduction to hydrodynamics and water waves. Springer Study Edition*. Springer.

Lentz, S. J., Churchill, J. H., Davis, K. A., & Farrar, J. T. (2016). Surface gravity wave transformation across a platform coral reef in the Red Sea. *Journal of Geophysical Research: Oceans*, *121*(1), 693–705. https://doi.org/10.1002/2015JC011142

Longuet-Higgins, M. S. (1953). Mass transport in water waves. *Philosophical Transactions of the Royal Society of London - Series A: Mathematical and Physical Sciences*, *245*(903), 535–581. https://doi.org/10.1098/rsta.1953.0006

Lowe, R. J., & Falter, J. L. (2015). Oceanic forcing of coral reefs. *Annual Review of Marine Science*, *7*(1), 43–66. https://doi.org/10.1146/annurev-marine-010814-015834

Lowe, R. J., Falter, J. L., Bandet, M. D., Pawlak, G., Atkinson, M. J., Monismith, S. G., & Koseff, J. R. (2005). Spectral wave dissipation over a barrier reef. *Journal of Geophysical Research*, *110*(C4), 273. https://doi.org/10.1029/2004JC002711

Lowe, R. J., Koseff, J. R., & Monismith, S. G. (2005). Oscillatory flow through submerged canopies: 1. Velocity structure. *Journal of Geophysical Research*, *110*(C10). https://doi.org/10.1029/2004JC002788

Lunt, J., Reustle, J., & Smee, D. L. (2017). Wave energy and flow reduce the abundance and size of benthic species on oyster reefs. *Marine Ecology Progress Series*, *569*, 25–36. https://doi.org/10.3354/meps12075

MacVicar, B., Dilling, S., Lacey, J., & Hipel, K. (2014). A quality analysis of the Vectrino II instrument using a new open-source MATLAB toolbox and 2D ARMA models to detect and replace spikes. In A. Schleiss, G. de Cesare, M. Franca, & M. Pfister (Eds.), *River flow 2014* (pp. 1951–1959). CRC Press. https://doi.org/10.1201/b17133-261

Madsen, O. S. (1994). Spectral wave-current bottom boundary layer flows. *Coastal Engineering Proceedings*, 384–398. https://doi.org/10.1061/9780784400890.030

Manis, J. E., Garvis, S. K., Jachec, S. M., & Walters, L. J. (2015). Wave attenuation experiments over living shorelines over time: A wave tank study to assess recreational boating pressures. *Journal of Coastal Conservation*, *19*(1), 1–11. https://doi.org/10.1007/s11852-014-0349-5

Markert, A. (2020). How dense is dense? Toward a harmonized approach to characterizing reefs of non-native Pacific oysters – With consideration of native mussels. *NeoBiota*, *57*, 7–52. https://doi.org/10.3897/neobiota.57.49196

Mathisen, P. P., & Madsen, O. S. (1996). Waves and currents over a fixed rippled bed: 1. Bottom roughness experienced by waves in the presence and absence of currents. *Journal of Geophysical Research*, *101*, 16533–16542. https://doi.org/10.1029/96JC00954

McClenachan, G. M., Donnelly, M. J., Shaffer, M. N., Sacks, P. E., & Walters, L. J. (2020). Does size matter? Quantifying the cumulative impact of small-scale living shoreline and oyster reef restoration projects on shoreline erosion. *Restoration Ecology*, *28*(6), 1365–1371. https://doi.org/10.1111/rec.13235

Mignot, E., Barthelemy, E., & Hurther, D. (2009). Double-averaging analysis and local flow characterization of near-bed turbulence in gravel-bed channel flows. *Journal of Fluid Mechanics*, *618*, 279–303. https://doi.org/10.1017/S0022112008004643

Mirfenderesk, H., & Young, I. R. (2003). Direct measurements of the bottom friction factor beneath surface gravity waves. *Applied Ocean Research*, *25*(5), 269–287. https://doi.org/10.1016/j.apor.2004.02.002

Monismith, S. G., Herdman, L. M. M., Ahmerkamp, S., & Hench, J. L. (2013). Wave transformation and wave-driven flow across a steep coral reef. *Journal of Physical Oceanography*, *43*(7), 1356–1379. https://doi.org/10.1175/JPO-D-12-0164.1

Monismith, S. G., Rogers, J. S., Koweek, D., & Dunbar, R. B. (2015). Frictional wave dissipation on a remarkably rough reef. *Geophysical Research Letters*, *42*(10), 4063–4071. https://doi.org/10.1002/2015GL063804

Monti, A., Nicholas, S., Omidyeganeh, M., Pinelli, A., & Rosti, M. E. (2022). On the solidity parameter in canopy flows. *Journal of Fluid Mechanics*, *945*, A17. https://doi.org/10.1017/jfm.2022.551

Morris, R. L., Konlechner, T. M., Ghisalberti, M., & Swearer, S. E. (2018). From grey to green: Efficacy of eco-engineering solutions for nature-based coastal defence. *Global Change Biology*, *24*(5), 1827–1842. https://doi.org/10.1111/gcb.14063

Morris, R. L., La Peyre, M. K., Webb, B. M., Marshall, D. A., Bilkovic, D. M., Cebrian, J., et al. (2021). Large-scale variation in wave attenuation of oyster reef living shorelines and the influence of inundation duration. *Ecological Applications*, *31*(6). https://doi.org/10.1002/eap.2382

Narayan, S., Beck, M. W., Reguero, B. G., Losada, I. J., Van Wesenbeeck, B., Pontee, N., et al. (2016). The effectiveness, costs and coastal protection benefits of natural and nature-based defences. *PLoS One*, *11*(5), e0154735. https://doi.org/10.1371/journal.pone.0154735

Nehring, S. (2011). Nobanis - invasive alien species fact sheet - Crassostrea gigas: From: Online database of the European network on invasive alien species - NOBANIS. Bonn, Germany. Retrieved from https://www.nobanis.org/globalassets/speciesinfo/c/crassostrea-gigas/crassostrea-gigas.pdf

Nelson, K. A., Leonard, L. A., Posey, M. H., Alphin, T. D., & Mallin, M. A. (2004). Using transplanted oyster (*Crassostrea virginica*) beds to improve water quality in small tidal creeks: A pilot study. *Journal of Experimental Marine Biology and Ecology*, *298*(2), 347–368. https://doi.org/10.1016/S0022-0981(03)00367-8

Nelson, R. C. (1996). Hydraulic roughness of coral reef platforms. *Applied Ocean Research*, *18*(5), 265–274. https://doi.org/10.1016/S0141-1187(97)00006-0

Nepf, H. M. (1999). Drag, turbulence, and diffusion in flow through emergent vegetation. *Water Resources Research*, *35*(2), 479–489. https://doi.org/10.1029/1998WR900069

Nepf, H. M. (2012). Hydrodynamics of vegetated channels. *Journal of Hydraulic Research*, *50*(3), 262–279. https://doi.org/10.1080/00221686.2012.696559

Nepf, H. M., & Vivoni, E. R. (2000). Flow structure in depth-limited, vegetated flow. *Journal of Geophysical Research*, *105*(C12), 28547–28557. https://doi.org/10.1029/2000JC900145

Newell, R. I. E. (1988). *Ecological changes in Chesapeake Bay: Are they the result of overharvesting the American oyster, Crassostrea virginica*. In M. P. Lynch & E. C. Crome (Eds.), *Understanding the estuary: Advances in Chesapeake Bay research (Proceedings of a conference, 29–31 March 1988, Baltimore, Maryland* (Vol. 129, pp. 536–546). CRC Publication.

Nielsen, P. (1992). *Coastal bottom boundary layers and sediment transport. Advanced Series on Ocean Engineering. Vol. 4*. World Scientific. https://doi.org/10.1142/1269

Nikora, V., McEwan, I., McLean, S., Coleman, S., Pokrajac, D., & Walters, R. (2007). Double-averaging concept for rough-bed open-channel and overland flows: Theoretical background. *Journal of Hydraulic Engineering*, *133*(8), 873–883. https://doi.org/10.1061/(asce)0733-9429(2007)133:8(873)

Nikuradse, J. (1933). Strömungsgesetze in rauhen Rohren. *VDI-Forschungsheft*, *361*(1).

Norris, B. K., Mullarney, J. C., Bryan, K. R., & Henderson, S. M. (2019). Turbulence within natural mangrove Pneumatophore Canopies. *Journal of Geophysical Research: Oceans*, *124*(4), 2263–2288. https://doi.org/10.1029/2018jc014562

Paul, M., & Amos, C. L. (2011). Spatial and seasonal variation in wave attenuation over *Zostera noltii*. *Journal of Geophysical Research*, *116*(C8), C08019. https://doi.org/10.1029/2010JC006797

Perry, A. E., Schofield, W. H., & Joubert, P. N. (1969). Rough wall turbulent boundary layers. *Journal of Fluid Mechanics*, *37*(2), 383–413. https://doi.org/10.1017/S0022112069000619

Petti, M., & Longo, S. (2001). Turbulence experiments in the swash zone. *Coastal Engineering*, *43*(1), 1–24. https://doi.org/10.1016/S0378-3839(00)00068-5

Pope, N. D., Widdows, J., & Brinsley, M. D. (2006). Estimation of bed shear stress using the turbulent kinetic energy approach—A comparison of annular flume and field data. *Continental Shelf Research*, *26*(8), 959–970. https://doi.org/10.1016/j.csr.2006.02.010

Pope, S. B. (2012). *Turbulent flows*. Cambridge University Press.

Ramponi, R., Blocken, B., De Coo, L. B., & Janssen, W. D. (2015). CFD simulation of outdoor ventilation of generic urban configurations with different urban densities and equal and unequal street widths. *Building and Environment*, *92*, 152–166. https://doi.org/10.1016/j.buildenv.2015.04.018

Raupach, M. R., & Shaw, R. H. (1982). Averaging procedures for flow within vegetation canopies. *Boundary-Layer Meteorology*, *22*(1), 79–90. https://doi.org/10.1007/BF00128057

Raushan, P. K., Paul, A., Singh, S. K., & Debnath, K. (2020). Spatially-averaged turbulent flow characteristics over ribbed surface in presence of unidirectional wave over steady current. *Applied Ocean Research*, *100*, 102154. https://doi.org/10.1016/j.apor.2020.102154

Reidenbach, M. A., Berg, P., Hume, A., Hansen, J. C. R., & Whitman, E. R. (2013). Hydrodynamics of intertidal oyster reefs: The influence of boundary layer flow processes on sediment and oxygen exchange. *Limnology & Oceanography*, *3*(1), 225–239. https://doi.org/10.1215/21573689-2395266

Reidenbach, M. A., Monismith, S. G., Koseff, J. R., Yahel, G., & Genin, A. (2006). Boundary layer turbulence and flow structure over a fringing coral reef. *Limnology & Oceanography*, *51*(5), 1956–1968. https://doi.org/10.4319/lo.2006.51.5.1956

Reise, K. (1998). Pacific oysters invade mussel beds in the European Wadden Sea. *Senckenbergiana Maritima*, *28*(4–6), 167–175. https://doi.org/10.1007/bf03043147

Reise, K., Buschbaum, C., Büttger, H., Rick, J., & Wegner, K. M. (2017). Invasion trajectory of Pacific oysters in the northern Wadden Sea. *Marine Biology*, *164*(4), 68. https://doi.org/10.1007/s00227-017-3104-2

Ribberink, J. S., & Al-Salem, A. A. (1995). Sheet flow and suspension of sand in oscillatory boundary layers. *Coastal Engineering*, *25*(3–4), 205–225. https://doi.org/10.1016/0378-3839(95)00003-T

Ridge, J. T., Rodriguez, A. B., & Fodrie, F. J. (2017). Evidence of exceptional oyster-reef resilience to fluctuations in sea level. *Ecology and Evolution*, *7*(23), 10409–10420. https://doi.org/10.1002/ece3.3473

Rodriguez, A. B., Fodrie, F. J., Ridge, J. T., Lindquist, N. L., Theuerkauf, E. J., Coleman, S. E., et al. (2014). Oyster reefs can outpace sea-level rise. *Nature Climate Change*, *4*(6), 493–497. https://doi.org/10.1038/NCLIMATE2216

Rogers, J. S., Monismith, S. G., Koweek, D. A., & Dunbar, R. B. (2016). Wave dynamics of a Pacific Atoll with high frictional effects. *Journal of Geophysical Research: Oceans*, *121*(1), 350–367. https://doi.org/10.1002/2015JC011170

Salvador de Paiva, J. N., Walles, B., Ysebaert, T., & Bouma, T. J. (2018). Understanding the conditionality of ecosystem services: The effect of tidal flat morphology and oyster reef characteristics on sediment stabilization by oyster reefs. *Ecological Engineering*, *112*, 89–95. https://doi.org/10.1016/j.ecoleng.2017.12.020

Scandura, P. (2007). Steady streaming in a turbulent oscillating boundary layer. *Journal of Fluid Mechanics*, *571*, 265–280. https://doi.org/10.1017/S0022112006002965

Schlichting, H. (1936). Experimental investigation of the problem of surface roughness. N.a.C.a. Technical Memorandum. (NACA-TM-823).

Scyphers, S. B., Powers, S. P., Heck, K. L., & Byron, D. (2011). Oyster reefs as natural breakwaters mitigate shoreline loss and facilitate fisheries. *PLoS One*, *6*(8), e22396. https://doi.org/10.1371/journal.pone.0022396

Seabrook, S. R., & Hall, K. R. (1998). Wave transmission at submerged rubblemound breakwaters. *Coastal Engineering Proceedings*, *1*, 2000–2013. https://doi.org/10.9753/icce.v26.%25p

Simons, R. R., Grass, T. J., & Mansour-Tehrani, M. (1993). Bottom shear stresses in the boundary layers under waves and currents crossing at right angles. In B. L. Edge (Ed.), *Coastal engineering 1992* (pp. 604–617). American Society of Civil Engineers. https://doi.org/10.1061/9780872629332.045

Sleath, J. F. A. (1987). Turbulent oscillatory flow over rough beds. *Journal of Fluid Mechanics*, *182*(-1), 369–409. https://doi.org/10.1017/S0022112087002374

Smaal, A. C., Ferreira, J. G., Grant, J., Petersen, J. K., & Strand, Ø. (2019). *Goods and services of marine bivalves*. Springer.

Soulsby, R. L. (1981). Measurements of the Reynolds stress components close to a marine sand bank. In C. A. Nittrouter (Ed.), *Developments in sedimentology*, *Sedimentary dynamics of continental shelves* (Vol. 32, pp. 35–47). Elsevier. https://doi.org/10.1016/S0070-4571(08)70293-0

Soulsby, R. L. (1983). Chapter 5: The bottom boundary layer of shelf seas. In B. Johns (Ed.), *Physical oceanography of coastal and shelf seas. Elsevier Oceanographic Series* (pp. 189–266). Elsevier. https://doi.org/10.1016/S0422-9894(08)70503-8

Soulsby, R. L. (1997). *Dynamics of marine sands. A manual for practical applications*. Thomas Telford Publications.

Stapleton, K. R., & Huntley, D. A. (1995). Seabed stress determinations using the inertial dissipation method and the turbulent kinetic energy method. *Earth Surface Processes and Landforms*, *20*(9), 807–815. https://doi.org/10.1002/esp.3290200906

Styles, R. (2015). Flow and turbulence over an oyster reef. *Journal of Coastal Research*, *31*(4), 978–985. https://doi.org/10.2112/JCOASTRES-D-14-00115.1

Sumer, B. M., & Fuhrman, D. R. (2020). *Turbulence in coastal and civil engineering. Advanced series on ocean engineering: Vol. 51*. World Scientific.

Swart, D. H. (1974). *Offshore sediment transport and equilibrium beach*. Delft Hydraulics Laboratory Publication. (131).

Thomas, R. E., Schindfessel, L., McLelland, S. J., Creëlle, S., & De Mulder, T. (2017). Bias in mean velocities and noise in variances and covariances measured using a multistatic acoustic profiler: The Nortek vectrino profiler. *Measurement Science and Technology*, *28*(7), 75302. https://doi.org/10.1088/1361-6501/aa7273

Thompson, C., Williams, J. J., Metje, N., Coates, L. E., & Pacheco, A. (2012). Turbulence based measurements of wave friction factors under irregular waves on a gravel bed. *Coastal Engineering*, *63*, 39–47. https://doi.org/10.1016/j.coastaleng.2011.12.011

Thornton, E. B., & Guza, R. T. (1983). Transformation of wave height distribution. *Journal of Geophysical Research*, *88*(C10), 5925–5938. https://doi.org/10.1029/JC088iC10p05925

Van Der A, D. A., Van Der Zanden, J., O'Donoghue, T., Hurther, D., Cáceres, I., Mclelland, S. J., & Ribberink, J. S. (2017). Large-scale laboratory study of breaking wave hydrodynamics over a fixed bar. *Journal of Geophysical Research: Oceans*, *122*(4), 3287–3310. https://doi.org/10.1002/2016JC012072

Van der Meer, J. W., Briganti, R., Zanuttigh, B., & Wang, B. (2005). Wave transmission and reflection at low-crested structures: Design formulae, oblique wave attack and spectral change. *Coastal Engineering*, *52*(10–11), 915–929. https://doi.org/10.1016/j.coastaleng.2005.09.005

Van Der Zanden, J., Van Der A, D. A., Cáceres, I., Hurther, D., Mclelland, S. J., Ribberink, J. S., & O'Donoghue, T. (2018). Near-bed turbulent kinetic energy budget under a large-scale plunging breaking wave over a fixed bar. *Journal of Geophysical Research: Oceans*, *123*(2), 1429–1456. https://doi.org/10.1002/2017JC013411

Van Rooijen, A., Lowe, R. J., Ghisalberti, M., McCall, R., & Hansen, J. E. (2022). Modelling wave attenuation through submerged vegetation canopies using a subgrid canopy flow model. *Coastal Engineering*, *176*, 104153. https://doi.org/10.1016/j.coastaleng.2022.104153

Van Rooijen, A., Lowe, R. J., Rijnsdorp, D. P., Ghisalberti, M., Jacobsen, N. G., & McCall, R. (2020). Wave-driven mean flow dynamics in submerged canopies. *Journal of Geophysical Research: Oceans*, *125*(3), 57. https://doi.org/10.1029/2019JC015935

Veenstra, J., Southwell, M., Dix, N., Marcum, P., Jackson, J., Burns, C., et al. (2021). High carbon accumulation rates in sediment adjacent to constructed oyster reefs, Northeast Florida, USA. *Journal of Coastal Conservation*, *25*(4), 40. https://doi.org/10.1007/s11852-021-00829-0

Walles, B., Mann, R., Ysebaert, T., Troost, K., Herman, P. M., & Smaal, A. C. (2015). Demography of the ecosystem engineer *Crassostrea gigas*, related to vertical reef accretion and reef persistence. *Estuarine, Coastal and Shelf Science*, *154*, 224–233. https://doi.org/10.1016/j.ecss.2015.01.006

Walles, B., Salvador de Paiva, J. N., Van Prooijen, B. C., Ysebaert, T., & Smaal, A. C. (2015). The ecosystem engineer *Crassostrea gigas* affects tidal flat morphology beyond the boundary of their reef structures. *Estuaries and Coasts*, *38*(3), 941–950. https://doi.org/10.1007/s12237-014-9860-z

Wehrmann, A., Herlyn, M., Bungenstock, F., Hertweck, G., & Millat, G. (2000). The distribution gap is closed — First record of naturally settled pacific oysters Crassostrea gigas in the East Frisian Wadden Sea, North Sea. *Senckenbergiana Maritima*, *30*(3), 153–160. https://doi.org/10.1007/bf03042964

Whitman, E. R., & Reidenbach, M. A. (2012). Benthic flow environments affect recruitment of *Crassostrea virginica* larvae to an intertidal oyster reef. *Marine Ecology Progress Series*, *463*, 177–191. https://doi.org/10.3354/meps09882

Wiberg, P. L., Taube, S. R., Ferguson, A. E., Kremer, M. R., & Reidenbach, M. A. (2019). Wave attenuation by oyster reefs in shallow coastal bays. *Estuaries and Coasts*, *42*(2), 331–347. https://doi.org/10.1007/s12237-018-0463-y

Wrange, A.-L., Valero, J., Harkestad, L. S., Strand, Ø., Lindegarth, S., Christensen, H. T., et al. (2010). Massive settlements of the Pacific oyster, *Crassostrea gigas*, in Scandinavia. *Biological Invasions*, *12*(5), 1145–1152. https://doi.org/10.1007/s10530-009-9535-z

Wright, L. D., Gammisch, R. A., & Bryne, R. J. (1990). Hydraulic roughness and mobility of three oyster-bed artificial substrate materials. *Journal of Coastal Research*, *6*(4), 867–978.

Yao, Y., Yang, X., Liu, W., & He, T. (2020). The effect of reef roughness on monochromatic wave breaking and transmission over fringing reefs. *Marine Georesources & Geotechnology*, *29*(3), 1–364. https://doi.org/10.1080/1064119X.2019.1702746

You, Z., Yin, B., & Huo, G. (2009). Direct measurement of wave-induced bottom shear stress under irregular waves. In C. Zhang & H. Tang (Eds.), *Advances in water Resources and hydraulic engineering* (pp. 1213–1218). Springer. https://doi.org/10.1007/978-3-540-89465-0_211

Young, I. R., & Gorman, R. M. (1995). Measurements of the evolution of ocean wave spectra due to bottom friction. *Journal of Geophysical Research*, *100*(C6), 10987–11004. https://doi.org/10.1029/94JC02563

Yuan, J., & Madsen, O. S. (2014). Experimental study of turbulent oscillatory boundary layers in an oscillating water tunnel. *Coastal Engineering*, *89*, 63–84. https://doi.org/10.1016/j.coastaleng.2014.03.007

Zhang, L., Zhang, F., Cai, A., Song, Z., & Tong, S. (2020). Comparison of methods for bed shear stress estimation in complex flow field of bend. *Water*, *12*(10), 2753. https://doi.org/10.3390/w12102753

Zhu, L., Chen, Q., Wang, H., Capurso, W., Niemoczynski, L., Hu, K., & Snedden, G. (2020). Field observations of wind waves in upper Delaware Bay with living shorelines. *Estuaries and Coasts*, *43*(4), 739–755. https://doi.org/10.1007/s12237-019-00670-7